Advances in Engineering Software 175 (2023) 103340

Contents lists available at ScienceDirect

Advances in Engineering Software

journal homepage: www.elsevier.com/locate/advengsoft

Research paper

A GPU-based 2D viscous flow model with variable density and heat exchange

Isabel Echeverribar [a,b,*], Sergio Martínez-Aranda [a], Javier Fernández-Pato [a,b], Pilar García-Navarro [a]

[a] Fluid Dynamic Technologies, i3A-Universidad de Zaragoza, Zaragoza, Spain
[b] Hydronia Europe, Madrid, Spain

ARTICLE INFO

Keywords:
Viscoplastic fluids
Thermally-driven geophysical flows
Finite volume methods
Riemann solvers
Variable density fluids
Temperature transport
Lava flow

ABSTRACT

Numerical simulation of unsteady viscous flow over variable topography under the influence of temperature changes is a challenge. In order to apply the model to large domains with complex topography, it becomes mandatory to reduce the model complexity from 3D to 2D by depth averaging the equations and to apply massive parallelization techniques for an efficient simulation. The depth averaged mass continuity, momentum and internal energy equations, combined with suitable friction laws, can be used for this type of flows. Variations in temperature can be accounted for from internal energy changes with density changing accordingly. The resulting system is solved using a finite volume technique on unstructured triangular grids well suited for problems over variable topography. A generic model applicable to a wide range of viscous fluids and validated with synthetic cases is presented to evaluate the performance of the numerical solution in presence of both external thermal forcing functions and discontinuous initial conditions. Finally, the model is applied to a realistic application and calibration to a particular case of lava flow taking into consideration variable density, viscosity and yield stress with temperature . A heat transfer with the air is included to consider the lava cooling. The numerical results of the lava front advance are compared to the Copernicus satellite observations at different dates. The efficiency of the GPU implementation allows to simulate a 11 day event in less than 1.7 h of simulation.

1. Introduction

Free surface geophysical flows include rivers and coastal or oceanic phenomena, as well as oil spills, landslides, mud or lava flows where a wide range of fluids and processes can be encountered. The most widely used approach is based on vertically averaged shallow models, assuming a hydrostatic pressure distribution in the fluid column and an incompressible flow hypothesis, thus discarding density variations that could affect the flow dynamics. Incompressibility is related with the assumption that pressure variations do not change the density, which, however, can still vary with temperature.

In rivers and coastal flows, temperature is often considered as a passively transported scalar with no influence on the flow [1,2]. Sometimes, if the interest is focused on buoyancy effects, the temperature is included to reproduce vertical motion [3], but not to reproduce horizontal waves generated by density discontinuities. Moreover, the effects of temperature variation on water quality reactions and substances [4,5] has also been studied. In other types of viscous incompressible flows the temperature analysis has been considered more relevant than the flow dynamics or the velocity field, which are often coarsely modelled or estimated as in [6–8] for river currents, [9–11] for lava flow or in [12,13] for overland oil spills. The technique of decoupling the resolution of the temperature transport equation from those of the flow dynamics provides good results in cases where the fluid does not reach high temperatures, such as environmental engineering problems related to water [2]. However, there are cases where the coupling between spatial and temporal temperature changes and fluid dynamics cannot be ignored so that a model that introduces this behaviour into the equations is required.

In the present work, a vertically averaged shallow flow model is presented that solves the fluid dynamics coupled with the internal energy equation by including density as one of the unknowns. Despite the simplifications assumed in the coupling process in the equations, an interesting aspect of the presented approach is that it maintains an unconditional hyperbolic character, that allows efficient numerical models capable of dealing with realistic large-scale and long-term geophysical events to be developed. By establishing a closure relationship that defines density as a function of temperature, the model will constitute a system for temperature-driven flows. Furthermore, the model will include not only density in the fundamental equations of

* Corresponding author at: Fluid Dynamic Technologies, i3A-Universidad de Zaragoza, Zaragoza, Spain.
E-mail address: echeverribar@unizar.es (I. Echeverribar).

https://doi.org/10.1016/j.advengsoft.2022.103340
Received 23 February 2022; Received in revised form 11 August 2022; Accepted 19 October 2022
Available online 14 November 2022

conservation of mass, momentum and energy, but also the influence of temperature on the rheological properties of the fluid. Temperature, as an additional variable, is solved by the internal energy conservation equation with a heat transfer source term causing temperature variations.

Numerical schemes in finite volumes have been developed in the last decades to solve systems of shallow water equations [2,14–17]. Well designed methods for the simulation of unsteady shallow flows including variable bed and friction have been a matter of research in recent times, and have provided different friction and bed slope discretization methods in the search of the most robust and efficient approach [15,18]. Among them, well balanced finite volume schemes have proved to be stable and robust in a wide range of test cases [15, 18,19], solving a traditional problem in the discretization of hyperbolic systems, such as the preservation of steady-states [20,21]. In this work, an explicit numerical scheme based on an upwind Riemann solver has been implemented as in [22], which has been extended to coupling with density following a procedure analogous to that of [23].

As in all explicit numerical schemes, the restriction of the time step through the CFL condition to ensure numerical stability poses a challenge to computational times when the models are applied to realistic cases. Recent efforts have been made to overcome this limitation as, for instance, Local Time Stepping (LTS) techniques [24]. In this work, efficiency is ensured by GPU acceleration [23].

The outline of the text is as follows: First, the governing equations are presented; then the main properties of the finite volume scheme used are outlined. The model is validated with theoretical test cases with reference solutions. The first two test cases consider separately the heat transfer and the effects of including density in the solver compared to a classical shallow water model, respectively. A third test case combines both effects with a modification of the rheological properties of the fluid. Then, this model is applied to a realistic lava flow, modelling heat transfer mechanisms and calibrating the fluid properties to validate a realistic phenomenon in an affordable computational time.

2. Governing equations

The depth averaged continuity equation is written as

$$\frac{\partial(\rho h)}{\partial t} + \frac{\partial}{\partial x}(\rho h u) + \frac{\partial}{\partial y}(\rho h v) = 0 \tag{1}$$

being ρ the depth-averaged bulk density [kg/m^3], h the vertical flow depth [m] and (u, v) the components of the depth-averaged flow velocity vector $\mathbf{u}$ [m/s]. Commonly the depth-averaged density ρ can be linearly related to the flow averaged temperature along the flow column T [°K] as

$$\rho(T) = \rho_0 + K(T - T_0) \tag{2}$$

where ρ_0 [kg/m^3] is the fluid reference density at the reference temperature T_0 [°K], and K [kg/(m^3·°K)] is a tuning constant.

The depth averaged equations for the bulk linear momentum along the $x-$ and $y-$coordinates can be expressed as

$$\frac{\partial(\rho h u)}{\partial t} + \frac{\partial}{\partial x}(\rho h u^2 + \frac{1}{2} g \rho h^2) + \frac{\partial}{\partial y}(\rho h u v) = -g\rho h \frac{\partial z_b}{\partial x} - \tau_{bx} \tag{3a}$$

$$\frac{\partial(\rho h v)}{\partial t} + \frac{\partial}{\partial x}(\rho h u v) + \frac{\partial}{\partial y}(\rho h v^2 + \frac{1}{2} g \rho h^2) = -g\rho h \frac{\partial z_b}{\partial x} - \tau_{by} \tag{3b}$$

being z_b the bed layer elevation [m] and (τ_{bx}, τ_{by}) the components of the depth-averaged basal resistance stress vector $\boldsymbol{\tau_b}[Pa]$, expressed as

$$\boldsymbol{\tau_b} = (\tau_{bx}, \tau_{by}) = \tau_b \, \mathbf{n_u} \tag{4}$$

with τ_b the modulus of the vector, and $\mathbf{n_u} = (n_{ux}, n_{uy})$ the direction given by the velocity unit vector. The formulation for the basal shear stress depends on the rheological law used. When turbulent flow states are considered, a quadratic relation on the depth-averaged velocity governs the basal resistance, that is modelled as

$$\tau_b = \rho g h C_f |\mathbf{u}|^2, \tag{5}$$

where $|\mathbf{u}| = \sqrt{u^2 + v^2}$ is the depth-averaged velocity modulus, and C_f is a friction coefficient. If the classical Manning's formula is chosen, this coefficient takes the form of a function of flow depth, h, and Manning roughness parameter, n_b [s·m$^{1/3}$], as

$$C_f = \frac{n_b^2}{h^{4/3}}. \tag{6}$$

On the other hand, for linear viscoplastic non-Newtonian flows, the Bingham law is used to model the behaviour of the flow as

$$2\tau_b^3 - 3\left(\tau_y(T) + 2\mu(T)\frac{|\mathbf{u}|}{h}\right)\tau_b^2 + \tau_y(T)^3 = 0 \tag{7}$$

where τ_y [Pa] and μ [Pa·s] stands for the bulk yield stress and plastic viscosity of the flow, respectively. Besides the flow density ρ, the depth-averaged temperature T affects directly viscosity and yield stress, provoking changes in the basal shear stress between the flow and the terrain. The formulation of these parameters as temperature functions considered here is based on [25] for the yield stress

$$\tau_y(T) = A_\tau + B_\tau \exp[C_\tau T], \tag{8}$$

where A_τ, B_τ and C_τ, are flow parameters coming from fluid characterization.

The assumed flow viscosity dependence with temperature is the Andrade formulation [26]

$$\mu(T) = A_\mu \exp(B_\mu / T), \tag{9}$$

where A_μ and B_μ are parameters to be determined in every case.

The depth-averaged temperature equation is derived from the internal energy equation that, neglecting horizontal diffusion and viscous dissipation, is written as

$$\frac{\partial(\rho h T)}{\partial t} + \frac{\partial}{\partial x}(\rho h u T) + \frac{\partial}{\partial y}(\rho h v T) = \frac{\dot{Q}}{C_p} \tag{10}$$

where $\dot{Q}$ [W/m^2] is the heat flux at the free surface and bed surface and C_p [J/(kg·K)] is the specific heat. They govern the temperature transfer between the flow and the surrounding media. The temperature Eq. (10) can be divided into a homogeneous and a non-homogeneous heat transport for convenience of numerical discretization (to be detailed later). The homogeneous part is expressed as

$$\frac{\partial(\rho h T)}{\partial t} + \frac{\partial}{\partial x}(\rho h u T) + \frac{\partial}{\partial y}(\rho h v T) = 0 \tag{11}$$

which can be rewritten as

$$\frac{\partial(h T)}{\partial t} + \frac{\partial}{\partial x}(h u T) + \frac{\partial}{\partial y}(h v T) = -h T \frac{1}{\rho}\frac{D\rho}{Dt} \tag{12}$$

where the term on the right hand side denotes the temperature change associated to the material derivative of density, i.e. the flow expansion. Considering (2), the normalized bulk density $r = \rho/\rho_0$ can be expressed as

$$r = 1 + \frac{K}{\rho_0}(T - T_0) \tag{13}$$

allowing to define the dimensionless normalized temperature T^∇ as

$$T^\nabla = \frac{K}{\rho_0}(T - T_0) \tag{14}$$

so the normalized density is rewritten as $r = 1 + T^\nabla$ and the flow depth can be expressed as $h = rh - hT^\nabla$. Using (13) and performing an estimation of the order of magnitude, the term on the right hand side of (12) can be neglected, and replacing (14) into (12), the transport equation for the dimensionless temperature can expressed as

$$\frac{\partial(hT^\nabla)}{\partial t} + \frac{\partial}{\partial x}(huT^\nabla) + \frac{\partial}{\partial y}(hvT^\nabla) = 0 \tag{15}$$

On the other hand, considering the non-homogeneous part of the energy Eq. (10) is written as

$$\frac{\partial(\rho h T)}{\partial t} = \frac{\dot{Q}}{C_p} \tag{16}$$

and, assuming $\partial(\rho h)/\partial t = 0$ to ensure mass conservation during the heat exchange process, the non-homogeneous time variations of temperature reduces to

$$\frac{\partial T}{\partial t} = \frac{\dot{Q}}{\rho h C_p} = \mathcal{S}_\mathcal{T} \tag{17}$$

The thermal source term $\mathcal{S}_\mathcal{T} = \dot{Q}/(\rho h C_p)$ can include different heat exchange mechanisms working along the vertical direction throughout the flow free surface, such as convection transfer produced by wind, heat increase due to the solar radiation, etc. In this work, these heat fluxes are directly set as external forcing functions, in order to assess the sensitivity of the model to them. However, this term might be divided into different heat sources representing different transfer mechanisms when simulating realistic cases, as in the last test case. The relative importance of the different heat transfer mechanisms is different depending on the fluid considered. When simulating lava flows, the emitted radiation is extremely relevant, as the fluid can be at a very high temperature. However, when simulation thin oil slicks, the emitted radiation might not be important, but the received radiation from sun would maintain its relatively high temperature for a longer time.

3. Numerical method

Therefore, the final system of equations to be solved is formed by: the mass (1) and momentum Eqs. (3a)– (3b) in terms of the normalized density r, the homogeneous part of the energy equation to transport the normalized temperature T^∇ (15), and the non-homogeneous part of temperature equations which contains the vertical thermal exchange (17). The system is completed with the closures for the normalized density r (13) and normalized temperature T^∇ (14).

The complete normalized system is solved in two steps. First, the system composed of the mass, momentum and homogeneous temperature transport equations is considered

$$\frac{\partial(rh)}{\partial t} + \frac{\partial}{\partial x}(rhu) + \frac{\partial}{\partial y}(rhv) = 0 \tag{18}$$

$$\frac{\partial(rhu)}{\partial t} + \frac{\partial}{\partial x}(rhu^2 + \frac{1}{2}grh^2) + \frac{\partial}{\partial y}(rhuv) = -grh\frac{\partial z_b}{\partial x} - \frac{\tau_{bx}}{\rho_0} \tag{19a}$$

$$\frac{\partial(rhv)}{\partial t} + \frac{\partial}{\partial x}(rhuv) + \frac{\partial}{\partial y}(rhv^2 + \frac{1}{2}grh^2) = -grh\frac{\partial z_b}{\partial x} - \frac{\tau_{by}}{\rho_0} \tag{19b}$$

$$\frac{\partial(hT^\nabla)}{\partial t} + \frac{\partial}{\partial x}(huT^\nabla) + \frac{\partial}{\partial y}(hvT^\nabla) = 0 \tag{20}$$

Eqs. (18), (19) and (20) can be written in a compact form, useful for the development of the finite volume method, as

$$\frac{\partial \mathbf{U}}{\partial t} + \nabla \cdot \mathbf{E}(\mathbf{U}) = \mathbf{S_b} + \mathbf{S_\tau} \tag{21}$$

where $\mathbf{U}$ is the conservative variables vector,

$$\mathbf{U} = \begin{pmatrix} rh & rhu & rhv & hT^\nabla \end{pmatrix}^T \tag{22}$$

$\mathbf{E} = \big(\mathbf{F}(\mathbf{U}), \mathbf{G}(\mathbf{U})\big)$ denote the conservative fluxes,

$$\mathbf{F} = \begin{pmatrix} rhu \\ rhu^2 + \frac{1}{2}grh^2 \\ rhuv \\ huT^\nabla \end{pmatrix}, \qquad \mathbf{G} = \begin{pmatrix} rhv \\ rhuv \\ rhv^2 + \frac{1}{2}grh^2 \\ hvT^\nabla \end{pmatrix}, \tag{23}$$

$\mathbf{S_b}$ represents the bed slope source term and $\mathbf{S_\tau}$ stands for basal resistance term.

$$\mathbf{S_b} = \begin{pmatrix} 0 \\ -grh(\partial z_b/\partial x) \\ -grh(\partial z_b/\partial y) \\ 0 \end{pmatrix}, \qquad \mathbf{S_\tau} = \begin{pmatrix} 0 \\ -(\tau_b/\rho_0)\, n_{ux} \\ -(\tau_b/\rho_0)\, n_{uy} \\ 0 \end{pmatrix}. \tag{24}$$

System (21) is solved using an explicit first-order Finite Volume (FV) scheme supported by a novel Riemann solver developed for the upwind computation of the numerical fluxes at the cell edges for thermally-driven compressible shallow flows. Once the homogeneous component of the system is solved, the heat exchange is incorporated into the solution in a second step by explicitly solving the non-conservative component of the temperature equation, (17) and reconstructing the characteristic flow features at the next time step.

3.1. Finite volume scheme for the conservative component

Following [23], a finite volume numerical scheme is derived by integrating the hyperbolic system (21) into a control volume, or computational cell Ω_i.

$$\frac{\mathrm{d}}{\mathrm{d}t}\int_{\Omega_i} \mathbf{U}\mathrm{d}\Omega + \int_{\Omega_i} \nabla \cdot \mathbf{E}(\mathbf{U})\mathrm{d}\Omega = \int_{\Omega_i} \mathbf{S}_b(\mathbf{U})\mathrm{d}\Omega + \int_{\Omega_i} \mathbf{S}_\tau(\mathbf{U})\mathrm{d}\Omega \tag{25}$$

By applying the Gauss theorem, the volume integral of convective fluxes can be transformed into a surface integral along the boundaries of the cell, leading to

$$\frac{\mathrm{d}}{\mathrm{d}t}\int_{\Omega_i} \mathbf{U}\mathrm{d}\Omega + \sum_{k=1}^{NE} \big(\mathbf{E}(\mathbf{U}) \cdot \mathbf{n}\big)_k l_k = \int_{\Omega_i} \mathbf{S}_b(\mathbf{U})\mathrm{d}\Omega + \int_{\Omega_i} \mathbf{S}_\tau(\mathbf{U})\mathrm{d}\Omega \tag{26}$$

where the sum is performed over the edges k, of a length l_k, that separate the cell Ω_i and its NE neighbouring cells (NE=3 in triangular meshes, NE=4 in square meshes), being $\mathbf{n}$ the outward unit normal vector at each cell edge.

In order to obtain a numerical solution from time t^n to time t^{n+1}, the cell averaged value of conservative variables $\mathbf{U}(x, y, t)$ at a cell i of area A_i at time t^n is expressed as

$$\mathbf{U}_i^n = \frac{1}{A_i}\int_{\Omega_i} \mathbf{U}(x, y, t)d\Omega \tag{27}$$

and an approximation of the source terms time integration at t^n can be defined as

$$\int_{\Omega_i} \mathbf{S_b}(\mathbf{U}_i^n)\mathrm{d}\Omega \approx \frac{1}{\Delta t}\int_{t^n}^{t^{n+1}}\int_{\Omega_i} \mathbf{S}_b(\mathbf{U})\mathrm{d}\Omega\mathrm{d}t \tag{28}$$

$$\int_{\Omega_i} \mathbf{S_\tau}(\mathbf{U}_i^n)\mathrm{d}\Omega \approx \frac{1}{\Delta t}\int_{t^n}^{t^{n+1}}\int_{\Omega_i} \mathbf{S}_\tau(\mathbf{U})\mathrm{d}\Omega\mathrm{d}t \tag{29}$$

Therefore, the finite volume method leads to the explicit updating scheme

$$\mathbf{U}_i^{n+1} = \mathbf{U}_i^n - \frac{\Delta t}{A_i}\sum_{k=1}^{NE}\big(\mathbf{E}(\mathbf{U}) \cdot \mathbf{n}\big)_k l_k + \frac{\Delta t}{A_i}\left(\int_{\Omega_i} \mathbf{S_b}(\mathbf{U}_i^n)\mathrm{d}\Omega + \int_{\Omega_i} \mathbf{S_\tau}(\mathbf{U}_i^n)\mathrm{d}\Omega\right) \tag{30}$$

and requires specific formulations for the discrete fluxes and source terms. In the present work they will be based on a well balanced approximate Riemann solver defined at the cell edges. For that purpose, it is beneficial to move to a rotated reference system [23,27]. The conservative flux matrix, $\mathbf{E}(\mathbf{U})$, satisfies the rotation invariant property [22,28]. That is, considering the local framework created by the normal $\mathbf{n} = (n_x, n_y)$ and tangential $\mathbf{t} = (-n_y, n_x)$ directions to kth cell edge, the associated rotation matrix $\mathbf{R}_k$ is defined as

$$\mathbf{R}_k = \begin{pmatrix} 1 & 0 & 0 & 0 \\ 0 & n_x & n_y & 0 \\ 0 & -n_y & n_x & 0 \\ 0 & 0 & 0 & 1 \end{pmatrix}_k \tag{31}$$

and the convective flux matrix $\mathbf{E}(\mathbf{U})$ satisfies

$$(\mathbf{E}(\mathbf{U}) \cdot \mathbf{n})_k = \big(\mathbf{F}(\mathbf{U})n_x + \mathbf{G}(\mathbf{U})n_y\big)_k = \mathbf{R}_k^{-1}\mathbf{F}(\mathbf{R}_k\mathbf{U}) \tag{32}$$

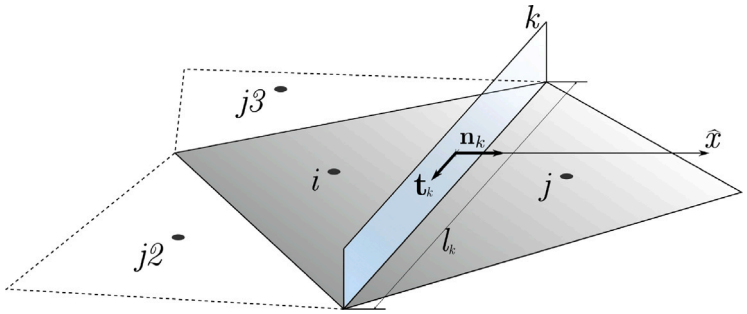

Fig. 1. Representation of the local framework built at the cell edge between cell i and its neighbour cell j.

where $\mathbf{R}_k^{-1}$ is the inverse matrix of $\mathbf{R}_k$. This approach allows to work within the local framework depicted in Fig. 1 for each kth cell edge, by defining the local conservative variables vector $\hat{\mathbf{U}}$ as

$$\hat{\mathbf{U}} \equiv \mathbf{R}_k \mathbf{U} = \left(rh,\ rhu_n,\ rhv_t,\ hT^{\nabla}\right)_k^T \tag{33}$$

being $u_n = \mathbf{u}\cdot\mathbf{n} = un_x + vn_y$ and $v_t = \mathbf{u}\cdot\mathbf{t} = -un_y + vn_x$ the normal and tangential projections of the velocity in the local edge framework respectively, and the local conservative flux vector $\mathbf{F}(\hat{\mathbf{U}})$ as

$$F(\hat{\mathbf{U}}) \equiv \mathbf{F}(\mathbf{R}_k\mathbf{U}) = \begin{pmatrix} rhu_n \\ rhu_n^2 + \frac{1}{2}grh^2 \\ rhu_n v_t \\ hu_n T^{\nabla} \end{pmatrix}_k \tag{34}$$

Additionally, to get an augmented scheme that includes the momentum source contributions into the numerical fluxes, both the bed slope and the basal resistance terms are split into local contribution as

$$\int_{\Omega_i} \mathbf{S_b}(\mathbf{U}_i^n)\mathrm{d}\Omega = \sum_{k=1}^{NE} \mathbf{R}_k^{-1}\mathbf{H}(\hat{\mathbf{U}})_k l_k \tag{35}$$

$$\int_{\Omega_i} \mathbf{S_\tau}(\mathbf{U}_i^n)\mathrm{d}\Omega = \sum_{k=1}^{NE} \mathbf{R}_k^{-1}\mathbf{T}(\hat{\mathbf{U}})_k l_k \tag{36}$$

where $\mathbf{H}(\hat{\mathbf{U}})_k$ and $\mathbf{T}(\hat{\mathbf{U}})_k$ are the bed slope and basal friction flux vectors, respectively, expressed in the local edge framework and defined as

$$\mathbf{H}(\hat{\mathbf{U}})_k = \begin{pmatrix} 0 \\ -g\widetilde{rh}\,\Delta z_b \\ 0 \\ 0 \end{pmatrix}_k \qquad \mathbf{T}(\hat{\mathbf{U}})_k = \begin{pmatrix} 0 \\ -\frac{\widetilde{\tau}_b}{\rho_0}\left(\widetilde{n}_{ux}\Delta x + \widetilde{n}_{uy}\Delta y\right) \\ 0 \\ 0 \end{pmatrix}_k \tag{37}$$

where $\widetilde{r}_k$, $\widetilde{h}_k$, $\widetilde{\tau}_{bk}$ and $(\widetilde{n}_{ux}, \widetilde{n}_{uy})_k$ are the edge-averaged quantities of the corresponding variable. that is $\widetilde{\langle\cdot\rangle}_k = (\langle\cdot\rangle_i^n + \langle\cdot\rangle_j^n)/2$, and $(\Delta z_b)_k$ and $(\Delta x, \Delta y)_k$ denotes the edge-increments of the corresponding variables, that is $(\Delta\langle\cdot\rangle)_k = \langle\cdot\rangle_j^n - \langle\cdot\rangle_i^n$. It is worth noting that, to ensure good properties, the momentum flux vectors $\mathbf{H}(\hat{\mathbf{U}})_k$ and $\mathbf{T}(\hat{\mathbf{U}})_k$ must satisfy the rotation invariant property [27].

Replacing (32), (35) and (36) into (30), the piecewise reconstruction of the conservative variables can be updated as

$$\mathbf{U}_i^{n+1} = \mathbf{U}_i^n - \frac{\Delta t}{A_i}\sum_{k=1}^{NE} \mathbf{R}_k^{-1}\left[\mathbf{F}(\hat{\mathbf{U}})_k - \mathbf{H}(\hat{\mathbf{U}})_k - \mathbf{T}(\hat{\mathbf{U}})_k\right] l_k \tag{38}$$

allowing to define an augmented flux vector $\boldsymbol{\mathcal{F}}_k^{\downarrow}$ through the kth cell edge which includes the convective fluxes and the momentum source contributions as

$$\boldsymbol{\mathcal{F}}_k^{\downarrow} = \left[\mathbf{F}(\hat{\mathbf{U}}) - \mathbf{H}(\hat{\mathbf{U}}) - \mathbf{T}(\hat{\mathbf{U}})\right]_k \tag{39}$$

In this work, the augmented flux vector is upwind computed using a novel 4-wave Riemann solver developed for thermally-driven compressible shallow flows (see Appendix) as

$$\boldsymbol{\mathcal{F}}_k^{\downarrow -} = \mathbf{F}(\hat{\mathbf{U}}_i^n) + \sum_{m-}\left[(\widetilde{\lambda}_m\widetilde{\alpha}_m - \widetilde{\beta}_m - \widetilde{\sigma}_m)\widetilde{\mathbf{e}}_m\right]_k^n \tag{40}$$

where $(\widetilde{\lambda}_m)_k^n$ are the wave celerities at the edge, i.e. the eigenvalues of the Jacobian matrix of the local Riemann problem (RP), $(\widetilde{\mathbf{e}}_m)_k^n$ are the eigenvectors of the RP, $(\widetilde{\alpha}_m)_k^n$ denotes the wave strengths accounting for the discontinuity on the local conservative variables, $(\widetilde{\beta}_m)_k^n$ are the source strengths which include the integrated bed slope contribution and $(\widetilde{\sigma}_m)^n$ are the source strengths which include the integrated basal resistance contribution through the cell edge. The subscript $m-$ under the sums indicates that only the waves travelling inward the i cell are considered, leading to the explicit upwind computation of the flux at the edge. Hence, the updating formula for the conservative variables can be reduced to

$$\mathbf{U}_i^{n+1} = \mathbf{U}_i^n - \frac{\Delta t}{A_i}\sum_{k=1}^{NE} \mathbf{R}_k^{-1}\boldsymbol{\mathcal{F}}_k^{\downarrow -} l_k \tag{41}$$

As an explicit numerical scheme is being used, an stability condition is needed to ensure a proper time step size, Δt. This value must be small enough to avoid the interaction between propagating waves and cell boundaries and is computed at each kth cell edge as

$$\Delta t_k = \frac{\min\left(A_i, A_j\right)}{l_k\ \max_m\left(|\widetilde{\lambda}_m|\right)_k^n} \tag{42}$$

and thus, the global time step size is limited by the Courant–Friedrichs–Lewy (CFL) condition as

$$\Delta t = \mathrm{CFL}\ \min_k \Delta t_k \tag{43}$$

bounding the CFL coefficient between 0 and 1 for 2D triangular meshes.

The global time step is dynamically controlled by the wave celerities given by the eigenvalues of the Jacobian matrix of the conservative fluxes preserving the scheme stability even for large density gradients and rapid flows. The upwind discretization of the source terms avoids additional time step reductions to ensure the stability of the solution regardless of the basal resistance formulation [29]. The numerical algorithm is implemented using GPU-acceleration techniques applied to compressible non-Newtonian shallow models, in order to generate an efficient simulation tool suitable for realistic large-scale long-term lava flow events without requiring the use of coarse meshes.

3.2. Non-conservative heat flux component

Once the value of the conservative variables ($\mathbf{U}$) at the i cell is updated with the homogeneous transport component, intermediate values for the primitive variables flow depth, depth-averaged temperature and flow density can be reconstructed as

$$h_i^* = (rh)_i^{n+1} - (hT^{\nabla})_i^{n+1} \tag{44a}$$

$$T_i^* = \frac{\rho_0}{K}\frac{(hT^{\nabla})_i^{n+1}}{(h)_i^*} + T_0 \tag{44b}$$

$$\rho_i^* = \rho_0 + K(T_i^* - T_0) \tag{44c}$$

The superscript * represents the fact that (44a), (44b) and (44c) do not provide the final updated variables. It is worth noting that the heat

exchange term has not been considered and, thus, neither flow depth, temperature nor density are the final updated variables at time t^{n+1} yet. The updated temperature is computed explicitly as

$$T_i^{n+1} = T_i^* + \Delta t\,(S_T)_i^n \tag{45}$$

where $(S_T)_i^n$ is the cell-centred heat exchange at the i cell for the time t^n, computed as

$$(S_T)_i^n = \frac{\dot{Q}_i^n}{\rho_0 (rh)_i^n C_p} \tag{46}$$

Therefore, the value of the flow density can be also updated with the new temperature field as

$$\rho_i^{n+1} = \rho_0 + K(T_i^{n+1} - T_0), \tag{47}$$

and, assuming that the heat flux does not modify the conservative flow mass at the cells, the final flow depth is updated as

$$h_i^{n+1} = \frac{\rho_0\,(rh)_i^{n+1}}{\rho_i^{n+1}} \tag{48}$$

Finally, the two-dimensional velocity field is calculated as

$$\begin{aligned} u_i^{n+1} &= \frac{(rhu)_i^{n+1}}{(rh)_i^{n+1}}, \\ v_i^{n+1} &= \frac{(rhv)_i^{n+1}}{(rh)_i^{n+1}}. \end{aligned} \tag{49}$$

4. Test cases and sensitivity analysis

The model has been first applied to synthetic test cases where the behaviour of the model can be analysed in detail and its correct operation can be validated. None of these test cases involve experimental data, field data or a practical application involving real values with a calibration process. The last case shows the application of the model to lava flow in a real volcano eruption.

4.1. Case 1: Radially-symmetrical paraboloid: heat transfer at rest

Having made the effort to formulate the governing equations as a system of conservation laws and having developed a well balanced finite volume method, we are interested in evaluating the ability of the proposed model to preserve equilibrium. In particular, the divided procedure to compute the fourth conserved variable, hT^{∇}, and later to update the temperature, T with the thermal source term must be validated. Therefore, the following test case is carried out to prove the thermal behaviour of the system in a case with exact solution. A paraboloid well filled with fluid at rest is cooled down until it reaches the air temperature. An analytical solution of the problem is calculated and compared with the numerical results of the model.

4.1.1. Reference solution

In this test case, a radially-symmetrical paraboloid is used to create a topography that leads to a non-homogeneous distribution of fluid depths following the radial function:

$$z_b(\xi) = \begin{cases} \alpha\xi^2 & \xi \le R \\ z_0 & \text{otherwise} \end{cases} \tag{50}$$

where $\alpha = z_0/R^2$, and ξ, as radial coordinate, is $\xi = \sqrt{(x-x_0)^2 + (y-y_0)^2}$.

During a given period of time, a thermal power, $\dot{Q}$ [W/m^2], is removed from the system provoking a decrease of temperature. For this case, a cooling function for heat transfer is chosen as follows:

$$\dot{Q} = -\gamma(T - T_A) \tag{51}$$

where γ is a chosen parameter and T_A is air temperature. The cooling law used here is a theoretical law that does not respond to any natural phenomenon, but to an intention to validate the model. Therefore, this function will provoke changes on temperature that, following Eq. (17), lead to:

$$\frac{\partial T}{\partial t} = -\frac{\gamma(T - T_A)}{\rho h C_p} = -\frac{\gamma(T - T_A)}{m(\xi) C_p} \tag{52}$$

where $m(\xi) = \rho h$ is a value that, although being a function of the paraboloid radius, ξ, remains constant in time due to mass conservation. Therefore, by integrating Eq. (52) between the initial condition and an arbitrary state,

$$\int_{T_0}^{T} \frac{1}{(T - T_A)}\mathrm{d}T = \int_{t_0}^{t} -\frac{\gamma}{m(\xi)C_p}\mathrm{d}t \tag{53}$$

provides a time function for temperature, assuming t_0=0:

$$T(\xi, t) = T_A + (T_0 - T_A)e^{-\frac{\gamma}{m(\xi)C_p}(t)} \tag{54}$$

and, by introducing (54) into the density definition (Eq. (2)), an analogous expression for density can be written:

$$\rho(\xi, t) = \rho_A + K(T_0 - T_A)e^{-\frac{\gamma}{m(\xi)C_p}(t)} \tag{55}$$

These two expressions, (54) and (55), will be used as reference solutions to compare with the numerical results. For that purpose, the analytical functions are projected into a square grid, $[i, j]$, that provides spatial distributions: $T_{ij}(t)$ and $\rho_{ij}(t)$, where both depend on m_{ij}, as:

$$\begin{aligned} T_{ij}(t) &= T_A + (T_0 - T_A)e^{-\frac{\gamma}{m_{ij}C_p}(t)} \\ \rho_{ij}(t) &= \rho_A + K(T_0 - T_A)e^{-\frac{\gamma}{m_{ij}C_p}(t)} \end{aligned} \tag{56}$$

On the other hand, mass and volume evolution must be also considered to ensure the proper behaviour of the model. Considering the topography function as in (50), the initial condition is defined as:

$$\begin{aligned} &t = t_0 = 0 \\ &T = T_0 \\ &\rho_0 = \rho_A + K(T_0 - T_A) \\ &h_0 = z_0 - z_b(\xi) = z_0 - \alpha\xi^2 \end{aligned} \tag{57}$$

and, thus, $m(\xi)$ will remain constant in time:

$$m(\xi) = m_0(\xi) = \rho_0 h_0 = \left[\rho_A + K(T_0 - T_A)\right](z_0 - \alpha\xi^2) \tag{58}$$

Analytically, the total mass can be computed as:

$$M(t) = \int_0^R \rho h 2\pi\xi \mathrm{d}\xi \tag{59}$$

and, due to mass conservation, it can be evaluated from the initial condition

$$M(t) = M_0 = \int_0^R \rho_0 h_0 2\pi\xi \mathrm{d}\xi = \int_0^R \rho_0 (z_0 - \alpha\xi^2) 2\pi\xi \mathrm{d}\xi \tag{60}$$

That finally reads:

$$M(t) = M_0 = \pi\rho_0 R^2 \left(z_0 - \frac{\alpha R^2}{2}\right) \tag{61}$$

Unlike mass, the volume will decrease during a cooling event and the reference curve can be also calculated for this case:

$$V(t) = \frac{M_0}{\int_0^R \rho(\xi, t)\mathrm{d}t} \rightarrow V(t) = \frac{M_0}{\sum_{ij} \rho_{ij}(t)} \tag{62}$$

Summarizing, a paraboloid topography can be used to describe a non-homogeneous topography leading to an spatial distribution of fluid depths, which will provoke an spatial distribution of temperatures if a cooling test in carried out over it. Reference expressions can be computed for the temporal and spatial evolution of temperature and volume and compared with the numerical results.

Table 1
Characteristics of the computational meshes used for Case 1 and RMSE on temperature and volume for the three analysed meshes.

Mesh	Mean cell area	N. cells	$RMSE_{T,t=20s}$	$RMSE_{T,t=200s}$	$RMSE_{T,t=500s}$	$RMSE_V$
M1	0.02 m^2	39923	0.9055	0.0717	0.0021	0.1392
M2	0.08 m^2	9928	1.7072	0.1586	0.0036	0.5608
M3	0.32 m^2	2432	4.1641	0.2511	0.0064	2.2669

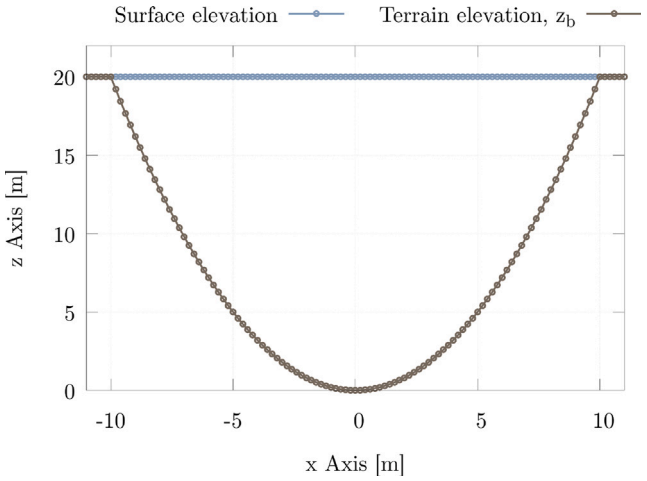

Fig. 2. Case 1: Initial condition of fluid surface elevation.

4.1.2. Test case description

For this case, a paraboloid of R = 11 m, a reference elevation of z_0 = 20 m and a coordinate origin $x_0 = 0$ and $y_0 = 0$ are chosen. These parameters are used to create a raster of 1 × 1 m, which is used to map the topography into three different unstructured computational meshes as summarized in Table 1. The reason is the interest in building a model able to work with unstructured triangular meshes well suited for irregular terrain.

The density expression (55) has been used with $\rho_A = 1000$ kg/m^3, $K = -1$ and $T_A = 0$ °C. Additionally, the initial temperature has been set to $T_0 = 200$ °C, γ=200 and C_p=1 J/(kgK).

All the boundaries are set as closed boundaries and the initial condition is a horizontal fluid surface elevation at rest, as seen in Fig. 2. A null viscosity is set to the fluid, together with an extremely high yield stress (in Eq. (7): A_τ=0; B_τ=200; C_τ=1), which avoids movement and focuses the case on heat transfer.

4.1.3. Numerical and reference results

The cooling test is simulated up to t=500 s with the three computational meshes. However, for the sake of clarity, only the comparison between the reference solution and the computational results is plotted in Fig. 3. The RMSE for the rest of the meshes is computed and shown in Table 1 for temperature and volume. The errors are computed following

$$RMSE_T = \sqrt{\frac{\sum(T_{ij}(t) - T_i(t))^2}{N_i}} \qquad RMSE_V = \sqrt{\frac{\sum(V(t^n) - V^n)^2}{N_n}} \quad (63)$$

for temperature and volume, respectively. In the temperature expression, N_i stands for the number of points in the x-profile where temperature is measured and T_ij and T_i for temperatures at profile points of the analytical and numerical solution, respectively, for a given time, t. For the volume error, computed along the simulation, N_n is the number of time steps where the volume of the numerical simulation, V^n, and the analytical solution, $V(t^n)$, have been compared for a given time, t^n. The reason why the RMSEs at different times differ so much is because the solution itself is time variable, with more marked gradient at the beginning and tendency to become smooth as time progresses.

More specifically, in Fig. 3(a), the comparison of the temporal evolution between the reference solution, computed following (62), and the numerical results obtained with the model can be seen. The volume exhibits an asymptotic behaviour, as it shows a steeper slope at the beginning, provoked by a heat transfer that depends on the temperature difference with the atmosphere, and a tendency to a constant volume at the end, where the heat transfer is almost non-existent. This behaviour is properly reproduced by the model and presents a good agreement with the reference solution.

On the other hand, in Fig. 3(b), the temperature profile along the x axis is contrasted between the reference and the computational mesh M1 for different times. The initial condition can be seen with uniform T = 200 °C. After 10 s, the boundaries of the well are colder due to their small fluid depths, which provokes a higher influence of the heat transfer, while the centre is still hot with the highest depths. This effect continues along time slowing down, so that the temperature gradient at the well centre between 20 and 50 s is almost the same as the gradient between 100 and 200 s. This gradient temperature, that is smaller at the end, is the cause of the previously seen asymptotic behaviour of the volume. At the end, the temperature is 0 °C in the whole domain, heat transfer stops and the volume remains constant. In the same Fig. 3(b), a better agreement between the reference solution, plotted with solid lines, and the numerical results, presented with pointed lines, can be noticed as the mesh gets refined.

For the sake of clarity, only M1 has been plotted in Fig. 3. Coarser meshes could produce less accurate results in terms of temperature profile, leading even to a loss of symmetry if the mesh geometry marks the directions improperly.

Finally, in order to get a quantitative comparison, the RMSE is computed for the temperature profile and for temporal evolution of the volume for the three meshes. Table 1 summarizes these values, showing an acceptable agreement even with mesh M3 and better with M1 and M2. In all the meshes, the final solution presents better agreement than the early states. This effect is due to the trivial nature of the final solution, that provokes the higher accuracy even for the coarsest mesh. However, early states are more challenging for the model, presenting much better results with finer meshes.

4.2. Case 2: Dam-break over quiescent fluid at different temperature

A dam break over a quiescent fluid in a reservoir at a different temperature is carried out in order to analyse the effect of including the density within the system of equations in unsteady flow and allowing its variability to modify the wave propagation. The results of the model with the density included in the solver (as in system (21)), defined as *density formulation 1* (DF1), are compared with a classical shallow water model with a passive transport of temperature and density, named *density formulation 2* (DF2). Both models are used to simulate exactly the same test cases with the same computational mesh.

Two configurations are simulated using the same mesh, depth initial condition, and initial temperature values with the fluid in the column at T= 1000 °C, and the reservoir fluid initially at T= 0 °C. In sub-Case C2.1 the descending fluid column has initially a density of ρ = 2000 kg/m^3 and K=1 whereas in sub-case C2.2 the descending fluid column has initially a density of ρ = 3000 kg/m^3 and K=2. The density at the reservoir is 1000 kg/m^3 in both cases.

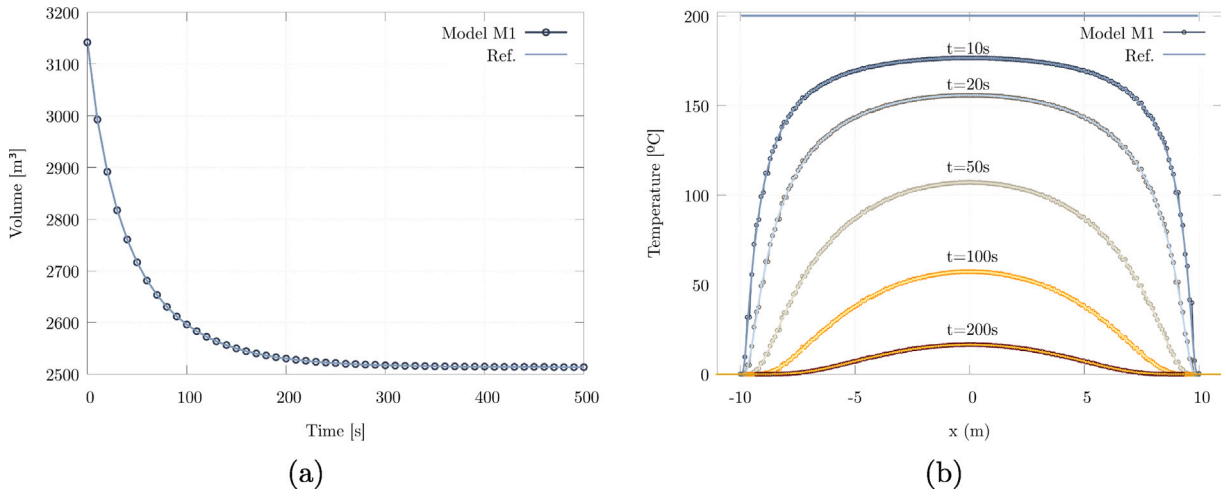

Fig. 3. Case 1: Comparison between the numerical results with mesh M1 and the reference solution in terms of temporal evolution of fluid volume (a) and temperature profile along x axis for different times (b).

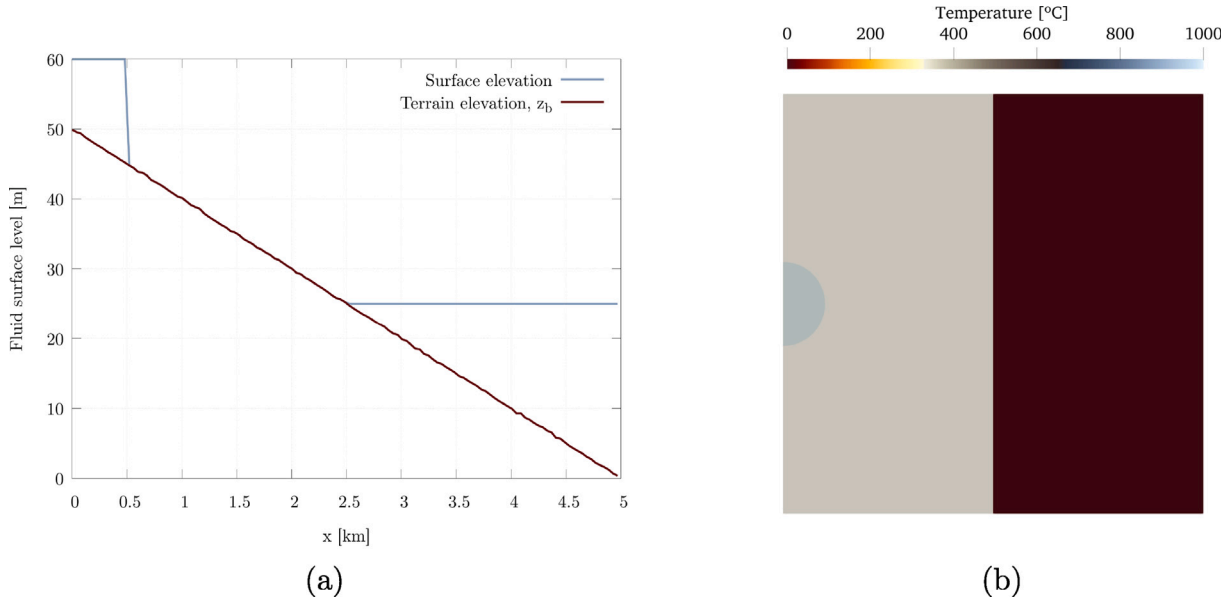

Fig. 4. Case 2: longitudinal profile of surface elevation (a) and top view of the temperature initial condition (b) for the dam break over quiescent reservoir test case.

4.2.1. Test case description

The topography and fluid surface initial conditions of the test case can be seen in Fig. 4(a), multiplied by a 20x scale factor for the sake of clarity. A top view of the temperature initial condition can be seen in Fig. 4(b).

Friction is modelled using the Manning formula (6) with a value n_b=0.025 $sm^{1/3}$. No heat losses are considered. An unstructured mesh is built with 37,863 triangular elements, boundaries are considered closed and the simulation runs up to t=480 s.

4.2.2. Numerical results

Fig. 5 shows the x profile of the fluid surface for both models at different times. It can be seen that the two models DF1 and DF2 provide exactly the same results until t=240 s. This is provoked by the fact that the moving wave presents at the beginning a homogeneous temperature distribution and, thus, in DF1 there are no waves generated by any density discontinuity and its results are the same as in a classical hydrodynamical model. However, when the dam-break wave reaches the quiescent reservoir, which is at a different temperature and density, discontinuities generate different waves and provoke different behaviour, as seen in Fig. 5 for t = 480 s. Since density changes affect the model when this variable is included into the solver (DF1), sub-cases C2.1 and C2.2 provide different results because the generated waves are different. However, the figure also shows how this variation of the initial condition does not generate any change in a classical shallow water model (DF2), as the density is only transported as a passive scalar.

This behaviour can be also seen when densities and velocities are analysed. Once the wave has reached the quiescent reservoir, the resultant velocity field is different depending on the model and the base density, as seen in Fig. 6. In the (a) image of the figure, the different density discontinuities between sub-case C2.1 and sub-case C2.2 can be seen. As each of the cases is resolved with the two different formulations, four different curves of density are shaped. However, velocities have a different behaviour as seen in Fig. 6(b). As DF2 is independent of density, it provides the same results for both cases, while DF1, besides being faster in both cases, the velocity wave depends on the fluid density.

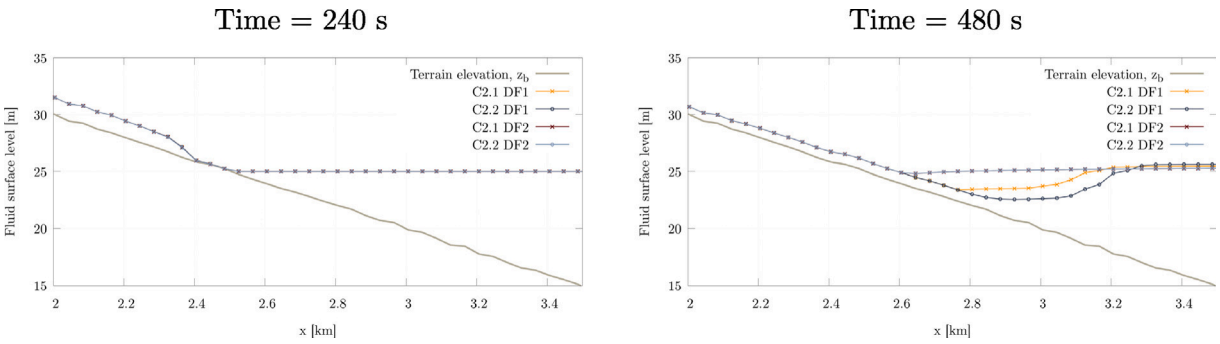

Fig. 5. Case 2: Flow free surface along x axis before and after the dam-break wave reaches the quiescent reservoir.

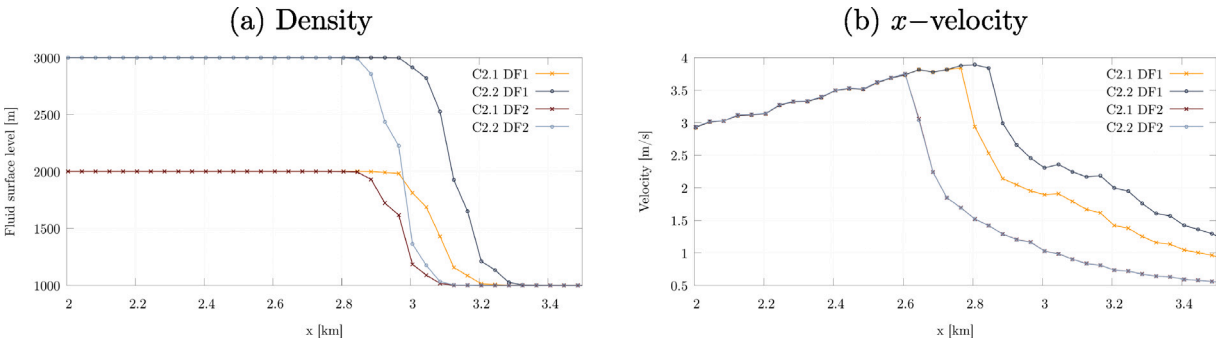

Fig. 6. Case 2: Longitudinal profile along x axis of (left) density and (right) x-velocity at $t = 480$ s in the dam-break over quiescent reservoir test case.

Table 2
Case 3: Chosen parameters to create raster for the mound topography.

R	5000.0 m	A	50.0	x_0	0.0 m
z_0	0.0	B	−0.0028	y_0	0.0 m

4.3. Case 3: Dam-break over a terrain mound with heat transfer

4.3.1. Test case description

In order to assess the model sensitivity to heat losses and fluid behaviour simultaneously, an initial water column with a cylindrical shape at the top of a mound is released, provoking a radial expansion of the fluid slick. The differences between an adiabatic case (without heat transfer) and a cooling case are considered in order to see the effects on the flow progress.

The topography is created following a cone function as

$$z(x,y) = \begin{cases} A\cos^2(B2\pi\xi) & \xi \le R \\ z_0 & \text{otherwise} \end{cases} \tag{64}$$

where $\xi = \sqrt{(x-x_0)^2+(y-y_0)^2}$. The function (64) is used with parameters of Table 2 to create a raster with Δx=1.0 m. An unstructured mesh is used with 316,479 triangular elements with a terrain elevation mapped from the raster that can be seen in Fig. 7(a). It is important to note that the 3D representation of the terrain is z scaled by 50x for the sake of clarity in visualization. The initial condition along the longitudinal x profile can be seen in Fig. 7(b). All the boundaries are closed.

For this case, friction is modelled with the Bingham law (see Eq. (7)). For yield stress, parameters are: A_τ=1, B_τ=2000 and C_τ=−0.3. Viscosity is computed with: A_μ=0.08 and B_μ=1200, following Eqs. (8) for yield stress and (9) for viscosity. The fluid is assumed to have the following parameters relating temperature and density according to (2): $K = 1$, $T_0 = 0$ °C, and $\rho_0 = 800$ kg/m^3. The parameters used for this test case are theoretical to allow a clear analysis in an extreme case.

Two different heat exchange situations are considered that give rise to two different test sub-cases: case 3.1, adiabatic case without heat losses ($\dot{Q}$=0 W/m^2) and case 3.2, with negative heat transfer ($\dot{Q}$=−100.0 W/m^2) cooling the fluid to air temperature (0 °C). The simulation runs up to t=10 h and the extension of the longitudinal profile of fluid surface is analysed and compared. Finally, in order to assess the method convergence a sensitivity analysis is performed over different computational meshes with a varying refinement.

4.3.2. Numerical results

Fig. 8 shows the longitudinal profile of surface level (a) and fluid depth (b) along the x axis for different times in both cases, the adiabatic and the cooling test case. All of them together with the initial fluid condition. Gravity governs the first hour of simulation provoking almost the same behaviour in both cases. However, the maximum extension of the cooling case (3.2) is reached at t=1 h and does not change for the rest of simulation. The adiabatic front (3.1) extends slightly further than the previous one, but it also reaches its maximum before the simulation ends, as profiles at t=5 h and t=10 h are almost the same.

For the last states, the non-homogeneous spatial distribution of depth provokes different intensity of heat transfer and, thus, develops a non-homogeneous spatial distribution of temperature, specially on the wave front. Additionally, due to the high effect of the source term depending on the depth, following (17), thin zones in the front cool down up to lower temperatures faster than the slick core, which presents higher fluid depths and preserves the initial temperature more time.

The method convergence is assessed through a sensitivity analysis that has been carried out simulating the sub-case 3.1 with different grid refinements. The used meshes, whose characteristics are summarized in Table 3, are selected varying the mean area of the triangular elements as they are unstructured (A). In the absence of an analytical solution, the numerical results obtained with a very fine mesh are considered as a reference (A=500m^2). The comparison is performed for t = 72 s.

The comparison of fluid depth is done by mapping the reference solution obtained by the reference mesh over the different meshes (from 1 to 6) generating a reference solution ($h_{i,ref}$) for each mesh at a given time, n. Then, fluid depth numerical results (h_i) are compared

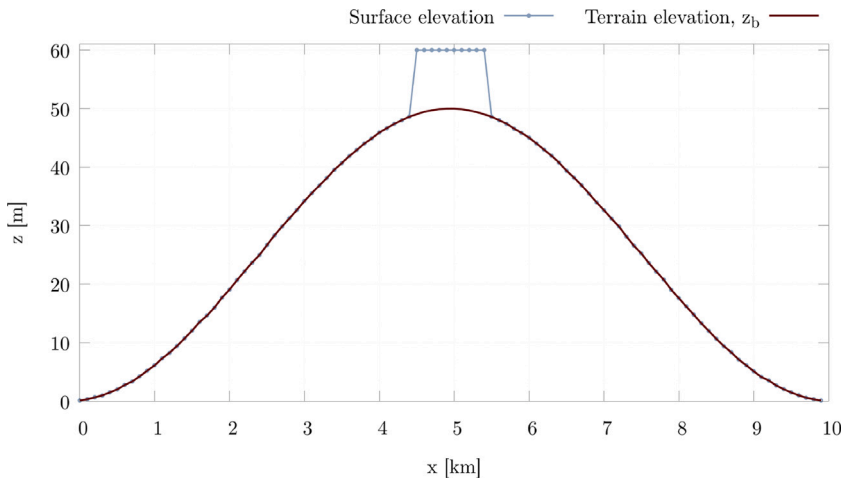

Fig. 7. Case 3: initial condition of fluid surface elevation.

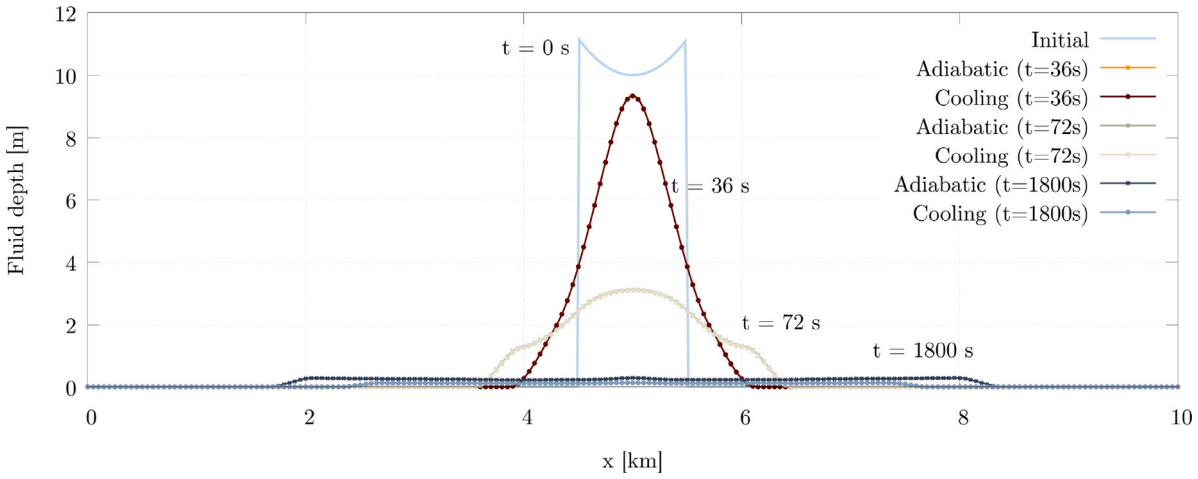

Fig. 8. Case 3: Longitudinal evolution of fluid depth along x axis for the adiabatic (-×-) and cooling (-○-) cases at different times.

Table 3
Case 3: Mean area of elements (A) and number of cells (NC) of computational meshes used for sensitivity analysis performed for sub-case 3.1.

Mesh	Reference	M1	M2	M3	M4	M5	M6
A	500	1000	2000	4000	8000	16000	32000
NC	316479	163816	81761	40991	20575	10144	5124

cell by cell for each mesh through the Root Mean Square Error (RMSE) weighted with cell area (A_i):

$$RMSE_M^n = \sqrt{\frac{\sum_i (h_i^n - h_{i,ref}^n) A_i}{\sum_i A_i}} \tag{65}$$

where subindex M stands for the analysed mesh. The analysis is carried out for $t = 72$ s and the obtained RMSE depending on the number of cells can be seen in Fig. 9. Together with the RMSE of the computational results, the slope of a 1st order scheme error convergence is plotted in order to compare the behaviour of the solution. Results are consistent with the fact that the numerical method is of first order.

4.4. Case 4: Cumbre Vieja lava flow

La Palma island is the most north-westerly island of the Canary Islands (Spain). It is a volcanic ocean island with an area of 708 Km^2 and a total population of 85,840 inhabitants (at the end of 2020). All its geography is a result of the volcanic formation of the island, leading to a maximum peak height of 2400 m above the sea level. The southern part of La Palma is formed by the Cumbre Vieja, a volcanic ridge formed by numerous volcanic cones built of lava. After 50 years of inactivity, a fissure eruption took place in Cumbre Vieja, started on 19 September 2021, preceded by and earthquake swarm 8 days before. In the following week, more than 22,000 earthquakes were recorded. The eruption caused the evacuation of over 7000 people and destroyed more than 2000 buildings. Fig. 10 represents the data captured by the Copernicus Sentinel-2 mission on 30 September and processed in true colour, using the shortwave infrared channel to highlight the lava flow from the volcano erupting and its pathway to the spill into the Atlantic Ocean.

Fig. 11(a) shows the discrete domain considered together with some representative locations. The spatial discretization is done by means of a computational mesh consisting of 108,167 triangular elements, locally refined along the lava trajectory (Fig. 11(b)). The main goal of this test case is to calibrate the properties of the fluid considered (density, viscosity and yield stress) by comparing the extension of the simulated lava with the observations of the Copernicus satellite [30] at different times during the first 11 days after the beginning of the eruption, until the lava reached the Atlantic Ocean. During this period, two main lava sources (Fig. 11) were the main contributors to the lava effusive flow. The observed areas of consecutive lava patches have been compared, obtaining an average volume for every time interval that has made it possible to estimate the effusive lava flow (Fig. 12).

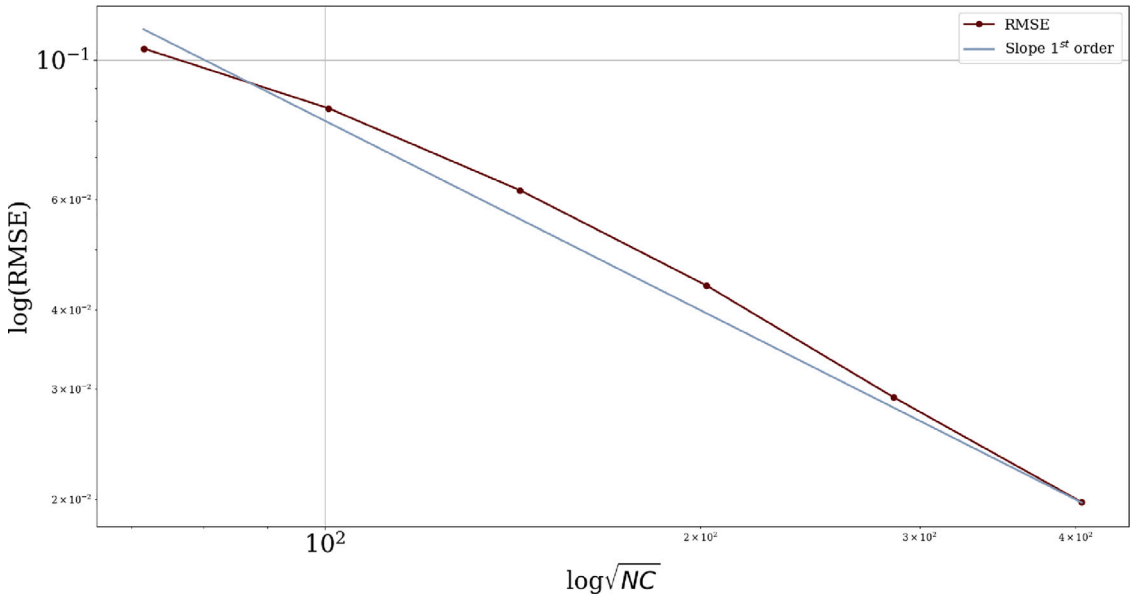

Fig. 9. Case 3: Computed RMSE as a function of the number of cells square root.

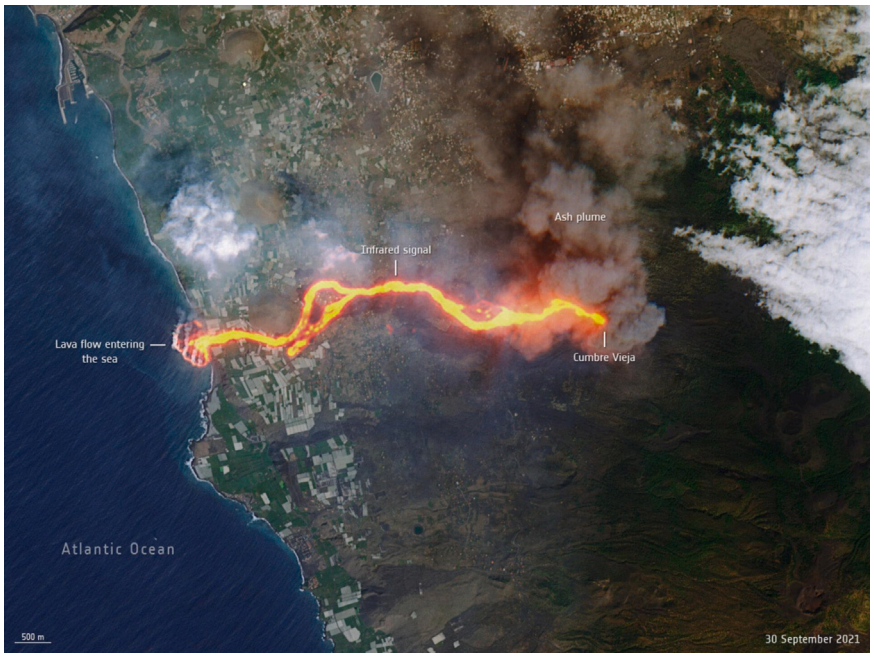

Fig. 10. Infrared image of the lava flow from the volcano erupting (Copernicus Sentinel data 2021, processed by European Space Agency (ESA)).

The temperature for the first source is set at 1100°C, whereas a hotter lava temperature from 1150°C to 1350°C is considered for the second source, as it is released from a lower region within the volcano cone due to the partial collapse of the northern wall.

4.4.1. Numerical results

For the application of the viscous model with variable temperature to a lava flow, the heat transfer is expressed as [31]

$$S_{\mathcal{T}} = \frac{\dot{Q}}{\rho h C_p} = \frac{\dot{Q}_{rad} + \dot{Q}_{conv}}{\rho h C_p} \tag{66}$$

The radiative heat transfer between the fluid and the air is computed by the Stefan–Boltzmann equation

$$\dot{Q}_{rad} = \epsilon\sigma \left(T^4 - T_{air}^4\right) \tag{67}$$

where ϵ is the fluid surface emissivity (assumed as 0.55 [32] for a lava flow), σ=5.67 $\cdot 10^{-8}$ W/(m^{2}K^{-4}) is the Stefan–Boltzmann constant and T_{air} is the air temperature.

On the other hand, the process of air convection is computed as a function of the difference between the fluid temperature, T, and the air temperature, T_{air} [K], and a convection coefficient, h_c,

$$\dot{Q}_{conv} = h_c \left(T - T_{air}\right) \tag{68}$$

in terms of the convective heat transfer coefficient h_c [Wm^{-2}K] that introduces the effect of air movement. It can be related to the Nusselt number, in order to establish how relevant is the convection heat transfer compared to the heat conduction:

$$Nu = \frac{h_c L}{k} \left(T - T_{air}\right) \tag{69}$$

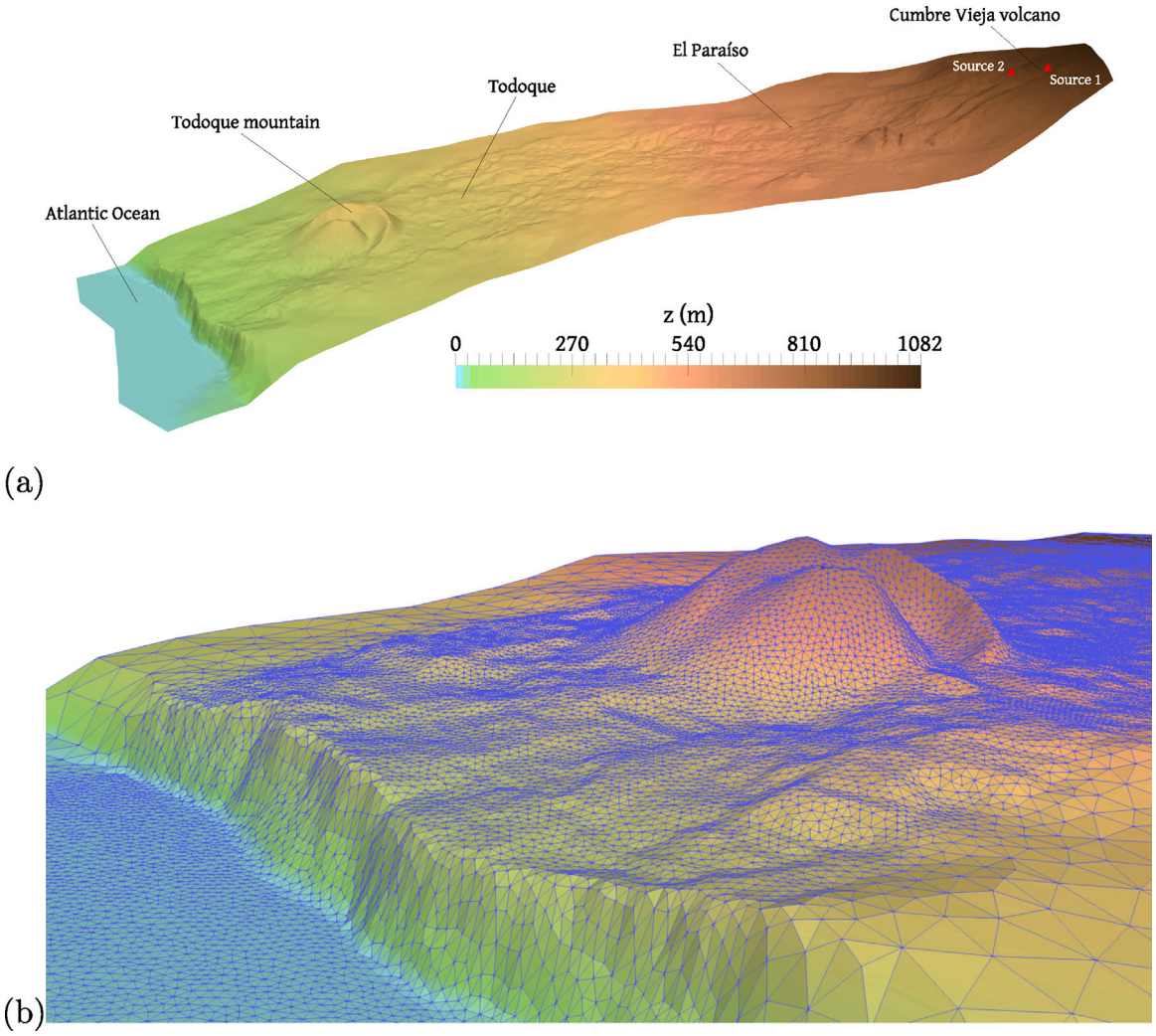

Fig. 11. (a) 3D representation of the bed level of the considered domain; (b) detail of the triangular unstructured computational mesh.

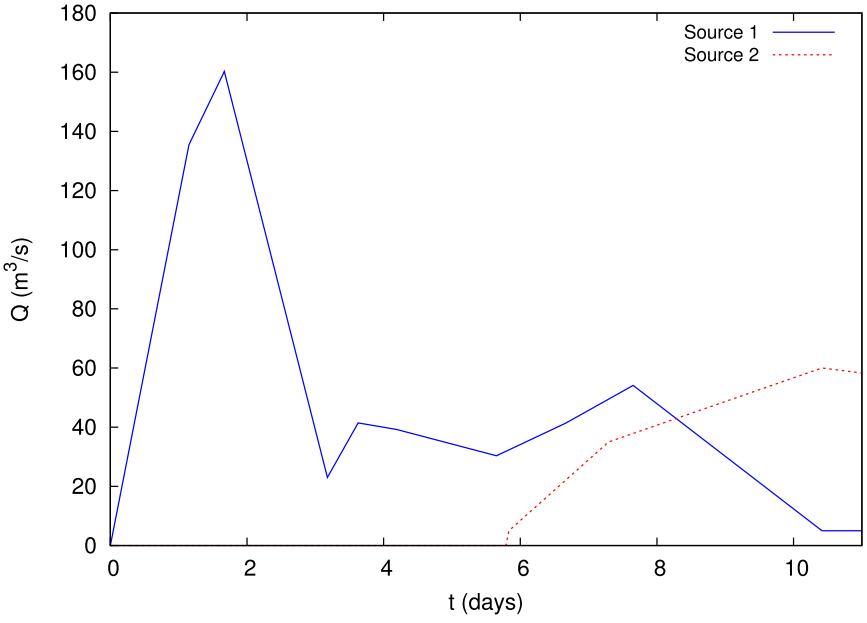

Fig. 12. Estimated effusive discharge for both lava sources.

Table 4
Density, yield stress and viscosity parameters.

K [kg/m^3 K]	A_τ [Pa]	B_τ [Pa]	C_τ [K^{-1}]	A_μ [Pa s]	B_μ [K^{-1}]
−0.1	0	$2.5{\cdot}10^6$	$4.29\ {\cdot}10^{-3}$	$2.0{\cdot}10^7$	$5.02\ {\cdot}10^{-3}$

Table 5
Obtained areas and F values for several times of the simulation.

t [h]	40	76	165	184	208	236
A_{num} [Km^2]	1.400	2.139	2.288	2.512	2.910	3.231
A_{obs} [Km^2]	1.586	1.776	2.409	3.114	3.131	3.860
$A_{num} \cap A_{obs}$ [Km^2]	1.158	1.486	1.704	1.970	1.925	2.319
$A_{num} \cup A_{obs}$ [Km^2]	1.825	2.426	2.993	3.207	3.639	4.299
F	0.634	0.613	0.569	0.614	0.529	0.539

Table 6
Computational times and GPU speed-up factor.

	CPU (1 core)	CPU (16 cores)	GPU-1	GPU-2
Comp. time (h)	477.19	33.37	6.88	1.65
Speed-up	–	14.3	69.4	289.2

being L [m] a characteristic length and k [W m/K] the thermal conductivity. A value of $h_c = 25$ W/(m^{2}K) is assumed in this work [32].

In addition to the correct estimation of the effusive flow, one of the main challenges when modelling the lava flow is the correct characterization of its physical properties. The lava density, viscosity, and yield stress present a strong dependency on the temperature which varies in a wide range throughout the descent of the lava. This variation in lava properties also affects the velocity of the lava propagation front. Hence, it is essential to carry out a correct characterization of the fluid properties. In this section, the calibration obtained for the parameters of the Eqs. (2), (8) and (9) is shown. This calibration is based on the fit of the distribution of the numerical lava layer to the extension of the observed field data, with the aim of reproducing the transitory lava flow as accurately as possible. Table 4 shows the density, yield stress and viscosity calibrated parameters for the present case. Figs. 13 and 14 show the results for the numerical lava flow overlapped with the satellite observations at $t = 40$ h and $t = 76$ h, respectively.

In order to find out the overall goodness of the fit, the feature agreement statistics performance measure proposed by [33] is used for all the available satellite data. This is a commonly used technique for validating extents produced by numerical flow models. It defines a dimensionless variable $F\,(0 \leq F \leq 1)$ that accounts for the intersection and union areas between the observed data (A_{obs}) and the numerical data (A_{num}) as follows:

$$F = \frac{A_{num} \cap A_{obs}}{A_{num} \cup A_{obs}} \tag{70}$$

Note that $F = 1$ stands for a perfect numerical and observed data match and $F = 0$ represents null coincidence. Table 5 shows the obtained F values for several times of the simulation.

Not only accurate but also fast numerical models are essential for hazard assessment and flow forecasting [34]. Therefore, the speed-up factor, defined as the ratio between the simulation time in CPU with a single core and the simulation time of a multi-core or GPU simulation, is shown in Table 6. The CPU simulations have been performed using an 16-core Intel Core i7-10700F at 2.90 GHz processor with 64 Gb of RAM, whereas NVIDIA GeForce GTX Titan Black (GPU-1) and NVIDIA A100 Tensor Core (GPU-2) devices have been used to run the GPU simulations.

5. Conclusions

In this work, a new formulation of a shallow water model for viscous flow influenced by temperature has been presented coupled to an energy equation in terms of temperature variations. This model allows not only to transport temperature as a passive value, but also to reproduce its influence on the momentum equations. A generic model of temperature-dependent flows has been developed that can be applied to a wide variety of fluids.

The resulting hyperbolic system represents a decisive advantage for developing robust and efficient numerical models capable of dealing with realistic large-scale and long-term geophysical events, despite the simplifications assumed in the coupling process in the equations. The augmented Riemann solver formulated has been designed to ensure mass conservative, well balanced numerical solutions even in presence of irregular beds and wet-dry fronts.

A test case for the cooling of a quiescent fluid, with reference solution, has been carried out to analyse the conservation of energy as a function of the action of this source term. It has been useful to see the ability of the numerical approximation to reproduce a basic thermal evolution in presence of variable depth.

Moreover, in order to analyse the influence of the inclusion of density within the solver, a test case of a dam break on a slope terminating in a reservoir with fluid at rest has been performed. It has been demonstrated that, if temperature is only transported as a passive scalar, waves generated by density discontinuities are not generated and the results can be different. Even using the simplest Manning friction law, very different results are observed at the moment when the dam break wave reaches the reservoir and there is a difference in densities. Thus, when trying to reproduce properly flows with strong density variations, this density must be introduced within the conserved variables vector, fluxes and numerical solver.

A detachment of a fluid column over a mound has been simulated under different heat transfer scenarios: adiabatic (no heat exchange) and cooling. The numerical solutions reproduce correctly the influence of the heat transfer on the front advance. This behaviour is observed in real flows such as oil spills or advancing lava flows, where the initial inertia forces, combined with high initial temperatures, allow the fluid to advance rapidly in the first instants and then, as the fluid cools, to advance more slowly as the viscosity and density increase.

Finally, the model has been applied to the first stage (11 days) of a real world event consisting of the recent eruption of Cumbre Vieja volcano, located in La Palma Island (Canary Islands, Spain).

Using data from Copernicus satellite the effluent discharge has been estimated and the propagation front has been tracked. As the lava density, viscosity, and yield stress affect the lava velocity propagation front, the parameters related to these fluid properties have been calibrated by fitting the numerical and observed lava patches all over the considered domain, taking into account their dependency with the temperature. This has required several runs of the model under different hypothesis. The numerical results have demonstrated that the model is robust and fast, making possible the simulation of all scenarios in an affordable time. In general, a good correspondence has been observed between the numerical results and the satellite observations, both in lava extension and in the propagation velocity of the lava front.

The results and conclusions obtained in this work support the need to develop accurate and efficient simulation models capable of predicting the path of viscous flows. The fluid properties are highly dependent on temperature, so its continuous monitoring is highly recommended. The efficiency of this type of distributed numerical models with hundreds of thousands or even millions of cells is based on the use of GPU devices for massive parallelization, obtaining speed-up factors >289x for the test cases presented in this work.

CRediT authorship contribution statement

Isabel Echeverribar: Conceptualization, Methodology, Software, Investigation, Validation, Writing – original draft. **Sergio Martínez-Aranda:** Conceptualization, Methodology, Software. **Javier Fernández-Pato:** Conceptualization, Methodology, Software. **Pilar García-Navarro:** Conceptualization, Methodology, Funding acquisition, Writing – review & editing.

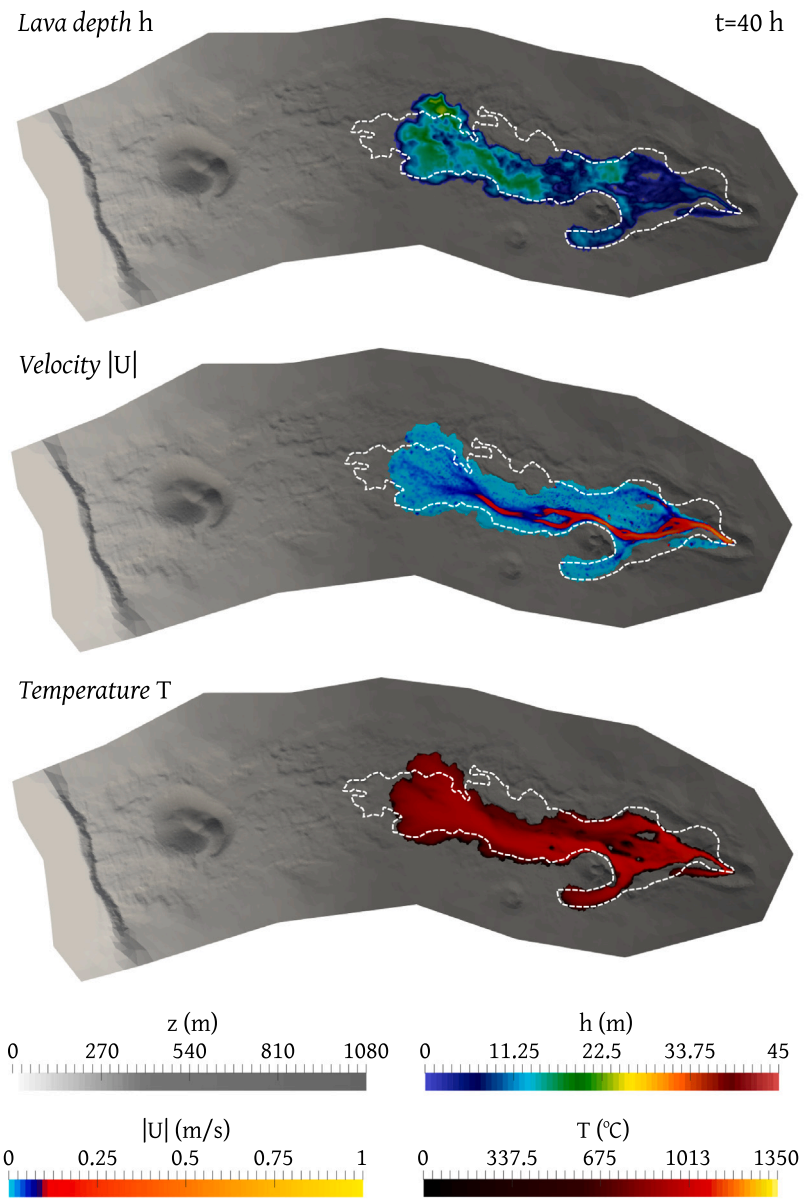

Fig. 13. Lava depth (upper), velocity (centre) and temperature (lower) over domain topography in grey scale at $t = 40$ h after the eruption. Comparison with satellite observations of the lava extension is also shown (dashed line).

Declaration of competing interest

The authors declare that they have no known competing financial interests or personal relationships that could have appeared to influence the work reported in this paper.

Acknowledgements

This work was partially funded by the Spanish Ministry of Science and Innovation under the research project PGC2018-094341-B-I00. This work has also been partially funded by Gobierno de Aragón, Spain through Fondo Social Europeo (T32-20R, Feder 2014–2020 "Construyendo Europa desde Aragón").

Appendix. Riemann solver for thermally-driven flows

In this section, a novel fully-coupled Riemann solver (RS) for thermally-driven compressible shallow flows is presented, based on the augmented RS previously developed for compressible mud/debris flows [23,35]. For the system of Eqs. (21), the approximate Jacobian matrix of the conservative fluxes expressed in the local framework of the kth cell edge can be defined as

$$\widetilde{\mathbf{J}}_k = \begin{pmatrix} 0 & 1 & 0 & 0 \\ \frac{1}{2}g\widetilde{h}\left(1+\widetilde{r}\right) - \widetilde{u}_n^2 & 2\widetilde{u}_n & 0 & -\frac{1}{2}g\widetilde{r}\widetilde{h} \\ -\widetilde{u}_n\widetilde{v}_t & \widetilde{v}_t & -\widetilde{u}_n & 0 \\ -\widetilde{u}_n\widetilde{T}^{\nabla}/\widetilde{r} & \widetilde{T}^{\nabla}/\widetilde{r} & 0 & \widetilde{u}_n \end{pmatrix}_k \tag{71}$$

and must satisfies

$$\delta\mathbf{F}(\hat{\mathbf{U}})_k = \widetilde{\mathbf{J}}_k\,\delta\hat{\mathbf{U}}_k \tag{72}$$

where $\delta\mathbf{F}(\hat{\mathbf{U}})_k = \mathbf{F}(\hat{\mathbf{U}}_j^n) - \mathbf{F}(\hat{\mathbf{U}}_i^n)$ and $\delta\hat{\mathbf{U}}_k = \hat{\mathbf{U}}_j^n - \hat{\mathbf{U}}_i^n$ denotes the increment on the local conservative fluxes and variables between cells Ω_i and Ω_j,

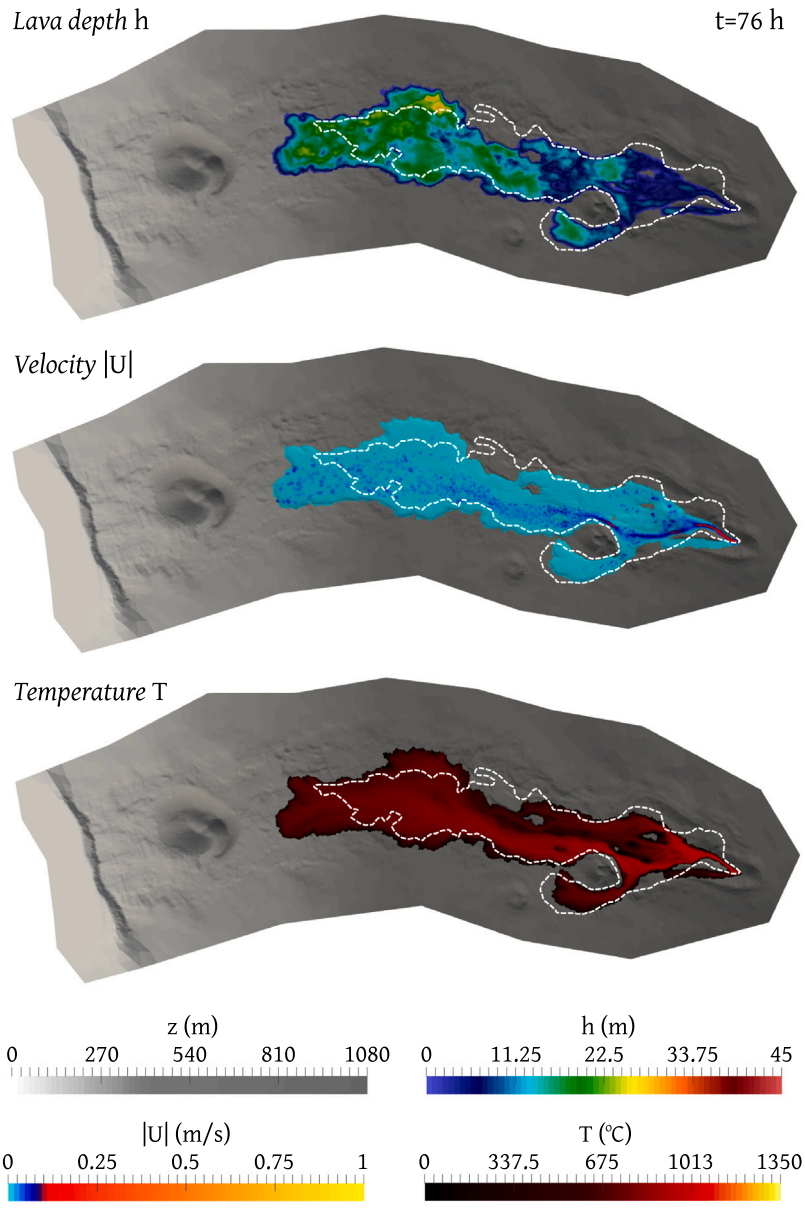

Fig. 14. Lava depth (upper), velocity (centre) and temperature (lower) over domain topography in grey scale at $t = 76$ h after the eruption. Comparison with satellite observations of the lava extension is also shown (dashed line).

allowing to define the wall-average values of the local variables as

$$\begin{aligned}
\widetilde{r} &= \frac{r_i h_i + r_j h_j}{h_i + h_j} \\
\widetilde{h} &= \frac{h_i + h_j}{2} \\
\widetilde{T}^{\nabla} &= \widetilde{r}\frac{T_i^{\nabla} h_i \sqrt{r_j h_j} + T_j^{\nabla} h_j \sqrt{r_i h_i}}{r_i h_i \sqrt{r_j h_j} + r_j h_j \sqrt{r_i h_i}}, \\
\widetilde{u}_n &= \frac{u_{n,i}\sqrt{r_i h_i} + u_{n,j}\sqrt{r_j h_j}}{\sqrt{r_i h_i} + \sqrt{r_j h_j}} \\
\widetilde{v}_t &= \frac{v_{t,i}\sqrt{r_i h_i} + v_{t,j}\sqrt{r_j h_j}}{\sqrt{r_i h_i} + \sqrt{r_j h_j}}
\end{aligned} \tag{73}$$

Analogous to the procedure detailed in [23] and due to the hyperbolic nature of the system, 4 real eigenvalues $\widetilde{\lambda}^m$ with $m = 1, \dots, 4$ can be obtained for the Jacobian matrix $\widetilde{\mathbf{J}}_k$ as

$$\widetilde{\lambda}_{1,k} = (\widetilde{u}_n - \widetilde{c})_k, \qquad \widetilde{\lambda}_{2,k} = (\widetilde{u}_n)_k, \qquad \widetilde{\lambda}_{3,k} = (\widetilde{u}_n + \widetilde{c})_k, \qquad \widetilde{\lambda}_{4,k} = (\widetilde{u}_n)_k. \tag{74}$$

being $\widetilde{c}_k$ the linearized flow celerity, defined as $\widetilde{c}_k = \left(\sqrt{\frac{1}{2} g \widetilde{h} \widetilde{m}}\right)_k$, where $\widetilde{m}_k = (1 + \widetilde{r} - \widetilde{T}^{\nabla})_k$.

The 4 associated eigenvectors $\widetilde{\mathbf{e}}_m$ compound the orthogonal basis of $\widetilde{\mathbf{J}}_k$ and are gathered into matrix $\widetilde{\mathbf{P}}_k = (\widetilde{\mathbf{e}}_1, \widetilde{\mathbf{e}}_2, \widetilde{\mathbf{e}}_3, \widetilde{\mathbf{e}}_4)_k$ that reads

$$\widetilde{\mathbf{P}}_k = \begin{pmatrix} 1 & 0 & 1 & \widetilde{r} \\ \widetilde{\lambda}_1 & 0 & \widetilde{\lambda}_3 & \widetilde{r}\widetilde{u}_n \\ \widetilde{v}_t & \widetilde{c} & \widetilde{v}_t & \widetilde{r}\widetilde{v}_t \\ \widetilde{T}^{\nabla}/\widetilde{r} & 0 & \widetilde{T}^{\nabla}/\widetilde{r} & 1 + \widetilde{r} \end{pmatrix}_k \tag{75}$$

which satisfies

$$\widetilde{\mathbf{J}}_k = (\widetilde{\mathbf{P}}\widetilde{\boldsymbol{\Lambda}}\widetilde{\mathbf{P}}^{-1})_k \qquad \widetilde{\boldsymbol{\Lambda}}_k = \begin{pmatrix} \widetilde{\lambda}_1 & & 0 \\ & \ddots & \\ 0 & & \widetilde{\lambda}_4 \end{pmatrix}_k \tag{76}$$

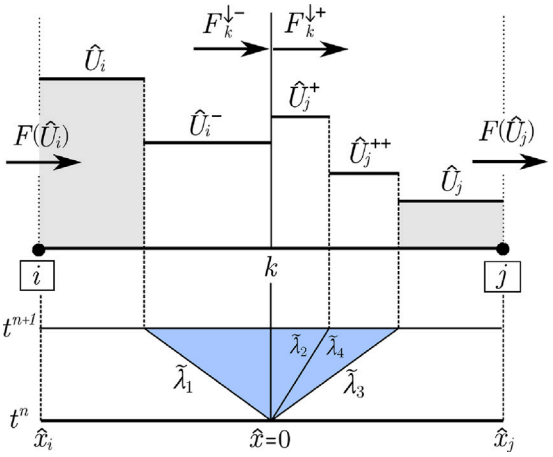

Fig. 15. Approximate solution for the local plane RP at the kth cell edge.

being $\widetilde{\mathbf{P}}_k^{-1}$ the inverse matrix of $\widetilde{\mathbf{P}}_k$.

The conservative variable increment $\delta\hat{\mathbf{U}}_k$ is projected on the eigenvector basis in order to obtain the wave strengths $\widetilde{\alpha}_{m,k}$ as

$$(\widetilde{\alpha}_1, \dots, \widetilde{\alpha}_4)_k^T = \widetilde{\mathbf{P}}_k^{-1}\,\delta\hat{\mathbf{U}}_k \quad \longrightarrow \quad \delta\hat{\mathbf{U}}_k = \sum_{m=1}^{4}(\widetilde{\alpha}_m\widetilde{\mathbf{e}}_m)_k \tag{77}$$

where $\widetilde{\alpha}_m$ are

$$\widetilde{\alpha}_1 = \frac{1}{2\widetilde{c}\widetilde{m}}\left[\delta(rh)\left((1+\widetilde{r})\widetilde{c} + \widetilde{m}\widetilde{u}_n\right) - \widetilde{m}\delta(rhu_n) - \widetilde{r}\widetilde{c}\delta(hT^{\nabla})\right] \tag{78a}$$

$$\widetilde{\alpha}_2 = \frac{1}{\widetilde{c}}\left[\delta(rh\widetilde{v}_t) - \widetilde{v}_t\delta(rh)\right] \tag{78b}$$

$$\widetilde{\alpha}_3 = \frac{1}{2\widetilde{c}\widetilde{m}}\left[\delta(rh)\left((1+\widetilde{r})\widetilde{c} - \widetilde{m}\widetilde{u}_n\right) + \widetilde{m}\delta(rhu) - \widetilde{r}\widetilde{c}\delta(hT^{\nabla})\right] \tag{78c}$$

$$\widetilde{\alpha}_4 = \frac{1}{\widetilde{m}}\left[\delta(\widetilde{h}\widetilde{T}^{\nabla}) - \frac{hT^{\nabla}}{\widetilde{r}}\delta(rh)\right] \tag{78d}$$

The bed slope and basal resistance momentum source terms are integrated into the numerical flux at the cell edges. The momentum edge-contributions $\mathbf{H}(\hat{\mathbf{U}})_{\mathbf{k}}$ and $\mathbf{T}(\hat{\mathbf{U}})_{\mathbf{k}}$ in (35) and (36) can be projected on the eigenvector basis in order to obtain the corresponding source strengths as

$$(\widetilde{\beta}_1, \dots, \widetilde{\beta}_4)_k^T = \widetilde{\mathbf{P}}_k^{-1}\,\mathbf{H}(\hat{\mathbf{U}})_k \quad \longrightarrow \quad \mathbf{H}(\hat{\mathbf{U}})_k = \sum_{m=1}^{4}(\widetilde{\beta}_m\widetilde{\mathbf{e}}_m)_k \tag{79a}$$

$$(\widetilde{\sigma}_1, \dots, \widetilde{\sigma}_4)_k^T = \widetilde{\mathbf{P}}_k^{-1}\,\mathbf{T}(\hat{\mathbf{U}})_k \quad \longrightarrow \quad \mathbf{T}(\hat{\mathbf{U}})_k = \sum_{m=1}^{4}(\widetilde{\sigma}_m\widetilde{\mathbf{e}}_m)_k \tag{79b}$$

and the source strengths reads

$$\widetilde{\beta}_1 = \frac{g\widetilde{r}\widetilde{h}\,\Delta z_b}{2\,\widetilde{c}} \qquad \widetilde{\sigma}_1 = \frac{\widetilde{\tau}_b\,(\widetilde{n}_{ux}\Delta x + \widetilde{n}_{uy}\Delta y)}{2\,\rho_0\,\widetilde{c}}$$

$$\widetilde{\beta}_2 = 0 \qquad \widetilde{\sigma}_2 = 0$$

$$\widetilde{\beta}_3 = -\frac{g\widetilde{r}\widetilde{h}\,\Delta z_b}{2\,\widetilde{c}} \qquad \widetilde{\sigma}_3 = -\frac{\widetilde{\tau}_b\,(\widetilde{n}_{ux}\Delta x + \widetilde{n}_{uy}\Delta y)}{2\,\rho_0\,\widetilde{c}}$$

$$\widetilde{\beta}_4 = 0 \qquad \widetilde{\sigma}_4 = 0$$

One result of Roe's linearization is that the approximate Riemann solution consists of only discontinuities and hence is governed by the wave celerities in $\widetilde{\lambda}_{m,k}$. Therefore, the approximate solution $\hat{\mathbf{U}}(\hat{x}, t)$ consists of four regions connected by 5 waves, one of them a contact wave with null celerity accounting for the integrated source term at the edge position $\hat{x} = 0$ (see Fig. 15).

According to the Godunov-type method, it is sufficient to provide the approximate solution at the intercell position $\hat{x} = 0$ in order to obtain the augmented numerical fluxes $\boldsymbol{\mathcal{F}}_k^{\downarrow}$ throughout the edge. Therefore, the definition of the numerical fluxes at the left and right sides, $\boldsymbol{\mathcal{F}}_k^{\downarrow-}$ and $\boldsymbol{\mathcal{F}}_k^{\downarrow+}$ respectively, of the kth cell edge is written as

$$\begin{aligned}\boldsymbol{\mathcal{F}}_k^{\downarrow-} &= \mathbf{F}(\hat{\mathbf{U}}_i^n) + \sum_{m-}\left[(\widetilde{\lambda}_m\widetilde{\alpha}_m - \widetilde{\beta}_m - \widetilde{\sigma}_m)\widetilde{\mathbf{e}}_m\right]_k^n \\ \boldsymbol{\mathcal{F}}_k^{\downarrow+} &= \mathbf{F}(\hat{\mathbf{U}}_j^n) - \sum_{m+}\left[(\widetilde{\lambda}_m\widetilde{\alpha}_m - \widetilde{\beta}_m - \widetilde{\sigma}_m)\widetilde{\mathbf{e}}_m\right]_k^n\end{aligned} \tag{80}$$

where the subscript $m-$ and $m+$ under the sums indicates waves travelling inward and outward the i cell.

Note that, when momentum source terms are incorporated into the Riemann solver, it is no longer possible to define a unique value of the numerical flux at both sides of the cell edge. The relation between the approximate fluxes $\boldsymbol{\mathcal{F}}_k^{\downarrow-}$ and $\boldsymbol{\mathcal{F}}_k^{\downarrow+}$ can be analysed using the Rankine–Hugoniot (RH) relation at $\hat{x} = 0$, which includes the steady contact wave accounting for the momentum sources. The corresponding flux jump is given by

$$\boldsymbol{\mathcal{F}}_k^{\downarrow+} - \boldsymbol{\mathcal{F}}_k^{\downarrow-} = \sum_{m=1}^{4}\left[(\widetilde{\beta}_m + \widetilde{\sigma}_m)\widetilde{\mathbf{e}}_m\right]_k^n = \mathbf{H}(\hat{\mathbf{U}})_k + \mathbf{T}(\hat{\mathbf{U}})_k \tag{81}$$

References

[1] Kim Kyung Sub, Chapra Steven C. Temperature model for highly transient shallow streams. J Hydraul Eng 1997;123(1):30–40.

[2] Cea L, Bermúdez M, Puertas J, Bladé E, Corestein G, Escolano E, et al. IberWQ: new simulation tool for 2D water quality modelling in rivers and shallow estuaries. J Hydroinform 2016;18(5):816–30.

[3] Hunt JCR, Fernando HJS, Princevac M. Unsteady thermally driven flows on gentle slopes. J Atmos Sci 2003;60(17):2169–82.

[4] Gordillo G, Morales-Hernández M, García-Navarro P. Finite volume model for the simulation of 1D unsteady river flow and water quality based on the WASP. J Hydroinform 2020;22(2):327–45.

[5] Gordillo G, Morales-Hernández M, Echeverribar I, Fernández-Pato J, García-Navarro P. A GPU-based 2D shallow water quality model. J Hydroinform 2020;22(5):1182–97.

[6] Gooseff Michael N, Anderson Justin K, Wondzell Steven M, LaNier Justin, Haggerty Roy. A modelling study of hyporheic exchange pattern and the sequence, size, and spacing of stream bedforms in mountain stream networks, Oregon, USA. Hydrol Process 2006;20(11):2443–57.

[7] Burkholder Barbara K, Grant Gordon E, Haggerty Roy, Khangaonkar Tarang, Wampler Peter J. Influence of hyporheic flow and geomorphology on temperature of a large, gravel-bed river, Clackamas River, Oregon, USA. Hydrol Process 2008;22(7):941–53.

[8] Dugdale SJ, Hanna DM, Malcolm IA. River temperature modelling: A review of process-based approaches and future directions. Earth-Sci Rev 2017;175:97–113.

[9] Fujita E, Nagai M. LavaSIM: its physical basis and applicability. In: Detecting, modelling and responding to effusive eruptions. London: Geological Society of London; 2016, p. 375–86.

[10] Harris AJ, Rowland S. FLOWGO: a kinematic thermo-rheological model for lava flowing in a channel. Bull Volcanol 2001;63:20–44.

[11] Rongo R, Lupiano V, Spataro W, D'ambrosio D, Iovine G, Crisci GM. SCIARA: cellular automata lava flow modelling and applications in hazard prediction and mitigation. In: Detecting, modelling and responding to effusive eruptions. London: Geological Society of London; 2016.

[12] Ramírez-Camacho JG, Carbone F, Pastor E, Bubbico R, Casal J. Assessing the consequences of pipeline accidents to support land-use planning. Saf Sci 2017;97:34–42.

[13] Chen C, Li C, Reniers G, Yang F. Safety and security of oil and gas pipeline transportation: A systematic analysis of research trends and future needs using WoS. J Clean Prod 2021;279:123583.

[14] Brufau P, García-Navarro P, Vázquez-Cendón ME. Zero mass error using unsteady wetting-drying conditions in shallow flows over dry irregular topography. Int J Numer Methods Fluids 2004;45(10):1047–82.

[15] Murillo J, Garcia-Navarro P. Weak solutions for partial differential equations with source terms: Application to the shallow water equations. J Comput Phys 2010;229(11):4327–68.

[16] Hubbard Matthew E, Dodd Nick. A 2D numerical model of wave run-up and overtopping. Coast Eng 2002;47(1):1–26.

[17] García-Navarro P, Murillo J, Fernández-Pato J, Echeverribar I, Morales-Hernández M. The shallow water equations and their application to realistic cases. Environ Fluid Mech 2019.

[18] Vázquez-Cendón ME. Improved treatment of source terms in upwind schemes for the shallow water equations in channels with irregular geometry. J Comput Phys 1999;148:497–8.

[19] Liang QH, Marche F. Numerical resolution of well-balanced shallow water equations with complex source terms. Adv Water Resour 2009;32:873–84.

[20] Leveque RJ. Finite volume methods fot hyperbolic problems. New York: Cambridge University Press; 2002.
[21] Toro EF. Shock-capturing methods for free-surface shallow flows. Wiley, New York; 2001.
[22] Murillo J, Navas-Montilla A. A comprehensive explanation and exercise of the source terms in hyperbolic systems using Roe type solutions. Application to the 1D-2D shallow water equations. Adv Water Resour 2016;98:70–96.
[23] Martínez-Aranda S, Murillo J, García-Navarro P. A GPU-accelerated efficient simulation tool (EST) for 2D variable-density mud/debris flows over non-uniform erodible beds. Eng Geol 2021;296:106462.
[24] Hu Peng, Zhao Zixiong, Ji Aofei, Li Wei, He Zhiguo, Liu Qifeng, et al. A GPU-accelerated and LTS-based finite volume shallow water model. Water 2022;14(6).
[25] Abdelraziq IR, Nierat TH. Rheology properties of castor oil: Temperature and shear rate-dependence of castor oil shear stress. J Mater Sci Eng 2015;5(1):1000220.
[26] da C. Andrade EN. XLI. A theory of the viscosity of liquids.—Part I. Lond Edinb Dublin Philos Mag J Sci 1934;17(112):497–511.
[27] Martínez-Aranda S. Efficient simulation tools (EST) for sediment transport in geomorphological shallow flows (Ph.D. thesis), Universiy of Zaragoza, Spain; 2021.
[28] Godlewski E, Raviart P-A. Numerical approximation of hyperbolic systems of conservation laws. New York: Springer-Verlag; 1996.
[29] Martínez-Aranda S, Murillo J, Morales-Hernández M, García-Navarro P. Novel discretization strategies for the 2D non-Newtonian resistance term in geophysical shallow flows. Eng Geol 2022. (submitted for publication).
[30] Copernicus Emergency Management Service. Directorate Space, Security and Migration, European Commission Joint Research Centre (EC JRC). 2021, https://emergency.copernicus.eu. [Accessed 07 October 2021].
[31] Patrick MR, Dehn J, Dean K. Numerical modeling of lava flow cooling applied to the 1997 Okmok eruption: Approach and analysis. J Geophys Res Solid Earth 2004;109(B3).
[32] Burgi PY, Caillet M, Haefeli S. Field temperature measurements at Erta'Ale Lava Lake, Ethiopia. Bull Volcanol 2002;64:472–85.
[33] Bates PD, De Roo APJ. A simple raster-based model for flood inundation simulation. J Hydrol 2000;236(1):54–77.
[34] Fernández-Pato J, Morales-Hernández M, García-Navarro P. Implicit finite volume simulation of 2D shallow water flows in flexible meshes. Comput Methods Appl Mech Engrg 2018;328:1–25.
[35] Martínez-Aranda S, Murillo J, García-Navarro P. A robust two-dimensional model for highly sediment-laden unsteady flows of variable density over movable beds. J Hydroinform 2020;22(5):1138–60.